



Published in final edited form as:

Cell Rep. 2023 January 31; 42(1): 111966. doi:10.1016/j.celrep.2022.111966.

The NLRP1 and CARD8 inflammasomes detect reductive stress

Qinghui Wang¹, Jeffrey C. Hsiao², Noah Yardeny³, Hsin-Che Huang³, Claire M. O'Mara¹, Elizabeth L. Orth-He³, Daniel P. Ball¹, Ze Zhang¹, Daniel A. Bachovchin^{1,2,3,4,*}

¹Chemical Biology Program, Memorial Sloan Kettering Cancer Center, New York, NY 10065, USA

²Pharmacology Program of the Weill Cornell Graduate School of Medical Sciences, Memorial Sloan Kettering Cancer Center, New York, NY 10065, USA

³Tri-Institutional PhD Program in Chemical Biology, Memorial Sloan Kettering Cancer Center, New York, NY 10065, USA

⁴Lead contact

SUMMARY

The danger signals that activate the related nucleotide-binding domain leucine-rich repeat pyrin domain-containing 1 (NLRP1) and caspase activation and recruitment domain-containing 8 (CARD8) inflammasomes have not been fully established. We recently reported that the oxidized form of TRX1 binds to NLRP1 and represses inflammasome activation. These findings suggested that intracellular reductive stress, which would reduce oxidized TRX1 and thereby abrogate the NLRP1-TRX1 interaction, is an NLRP1 inflammasome-activating danger signal. However, no agents that induce reductive stress were known to test this premise. Here, we identify and characterize several radical-trapping antioxidants, including JSH-23, that induce reductive stress. We show that these compounds accelerate the proteasome-mediated degradation of the repressive N-terminal fragments of both NLRP1 and CARD8, releasing the inflammasome-forming C-terminal fragments from autoinhibition. Overall, this work validates chemical probes that induce reductive stress and establishes reductive stress as a danger signal sensed by both the NLRP1 and CARD8 inflammasomes.

In brief

Wang et al. report small molecules that induce intracellular reductive stress. These molecules accelerate the degradation of the NLRP1 and CARD8 N-terminal repressive fragments, thereby potentiating inflammasome activation. These results strongly indicate that NLRP1 and CARD8 detect reductive stress.

This is an open access article under the CC BY-NC-ND license (<http://creativecommons.org/licenses/by-nc-nd/4.0/>).

*Correspondence: bachovcd@mskcc.org.

AUTHOR CONTRIBUTIONS

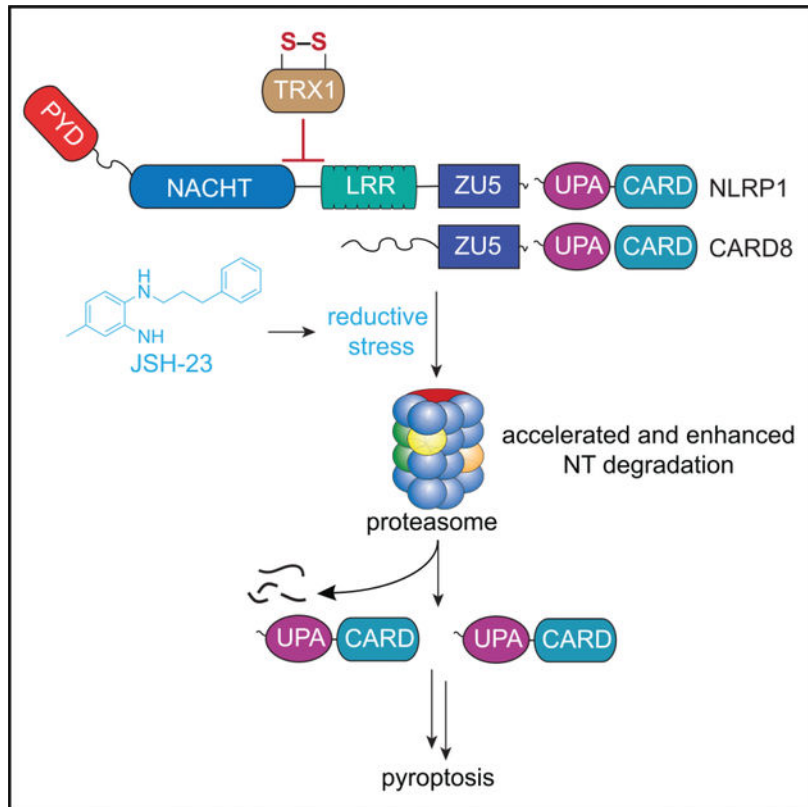
D.A.B. conceived and directed the project. Q.W., J.C.H., N.Y., H.-C.H., C.M.O., E.L.O.-H., D.P.B., and Z.Z. performed cloning, gene editing, biochemistry, and cell biology experiments. Q.W., J.C.H., N.Y., and H.-C.H. designed experiments and analyzed data. D.A.B. and Q.W. wrote the manuscript. All authors reviewed and provided input to the manuscript.

DECLARATION OF INTERESTS

MSKCC has filed for patent protection on behalf of D.A.B. and Q.W. for inventions relating to the induction of reductive stress.

SUPPLEMENTAL INFORMATION

Supplemental information can be found online at <https://doi.org/10.1016/j.celrep.2022.111966>.

Graphical Abstract:**INTRODUCTION**

Nucleotide-binding domain leucine-rich repeat pyrin domain-containing 1 (NLRP1) and caspase activation and recruitment domain-containing 8 (CARD8) are related human germline-encoded pattern-recognition receptors (PPRs) that sense intracellular danger signals, form multiprotein complexes called inflammasomes, and trigger caspase-1-dependent pyroptosis.^{1,2} Although recent research has greatly expanded our understanding of these receptors, the identities of the NLRP1- and CARD8-activating danger signals, and whether they are the same or different, have not yet been fully elucidated.³

NLRP1 and CARD8 have similar C-terminal regions that consist of function-to-find (FIIND) and CARD domains (Figure S1A). The FIINDs undergo autoproteolysis between ZU5 (ZO-1 and UNC5) and UPA (conserved in UNC5, PIDD, and ankyrin) subdomains, creating N-terminal (NT) and C-terminal (CT) fragments that remain non-covalently associated.⁴⁻⁶ The proteasome-mediated degradation of the NT fragments releases the CT fragments from autoinhibition in a process referred to as “functional degradation”^{7,8} (Figure S1B). Each freed CT fragment is then sequestered in a ternary complex with one copy of the full-length (FL) PRR and one copy of dipeptidylpeptidase 8 or 9 (DPP8/9), likely to prevent inflammasome formation during homeostatic protein turnover.⁹⁻¹² NLRP1 and CARD8 inflammasome-activating stimuli accelerate the rate of NT degradation and/or destabilize

the DPP8/9 ternary complex, thereby releasing a sufficient level of free CT fragments to self-oligomerize and form an inflammasome (Figure S1B).^{7,8,10–12}

The primordial functions of NLRP1 and CARD8 have not been definitively established. It is currently thought that they detect structures and/or activities of pathogens.¹³ Consistent with this idea, several pathogen-derived stimuli, including pathogen proteases, E3 ligases, and long double-stranded RNA (dsRNA), have been shown to activate NLRP1 and/or CARD8.^{7,14–18} However, none of these stimuli activate all NLRP1 alleles in humans and rodents (rodents do not have a CARD8 homolog), suggesting that each NLRP1 allele (as well as CARD8) may sense entirely distinct pathogen-associated features. Alternatively, it is possible that NLRP1 and CARD8 proteins sense a specific perturbation of a fundamental, but as-yet-unknown, aspect of cellular homeostasis.³ Supporting this idea, potent DPP8/9 inhibitors, including Val-boroPro (VbP), activate all functional NLRP1 and CARD8 proteins in humans and rodents by both accelerating the rate of NT degradation and destabilizing the DPP8/9 ternary complexes (Figure S1B).^{8–12,19–21} DPP8/9 are serine proteases that cleave XP dipeptides (X is any amino acid) from the N-termini of polypeptides.^{22–24} Intriguingly, XP peptides, which weakly bind to and inhibit DPP8/9, alone can activate the CARD8 inflammasome, suggesting they may be an endogenous danger-associated signal.²⁵ Based on these findings, we have hypothesized that NLRP1 and CARD8 evolved to sense a pathogen-induced “damage state” that is intimately related to DPP8/9 and XP peptides.^{3,25}

We recently discovered that stresses in addition to DPP8/9 inhibition likely contribute to this damage state as well. For example, we found that the non-selective metallo-aminopeptidase (AP) inhibitor bestatin methyl ester (MeBs), which induces the accumulation of many peptides (but generally not those with XP N termini) and thereby interferes with protein folding, accelerates the rate of NT degradation and synergizes with VbP to induce substantially more pyroptosis (Figure S1B).^{8,26} This work indicated that proteotoxic stress potentiates NLRP1 and CARD8 activation. Moreover, we recently uncovered evidence that NLRP1 senses a lack of reactive oxygen species (ROS) or reductive stress (Figure S1B). Briefly, NLRP1 has NT nucleotide-binding (NACHT) and leucine-rich (LRR) domains (Figure S1), and these domains associate with the oxidized form of thioredoxin-1 (TRX1).²⁷ We found that genetic loss of TRX1 sensitizes cells to VbP-induced pyroptosis, showing that oxidized TRX1 restrains NLRP1 activation. These results predicted that agents that deplete ROS and reduce TRX1 would synergize with VbP to induce more NLRP1-dependent pyroptosis. However, inducers of such reductive stress have not yet been identified and characterized. It should be noted that CARD8 does not have NT NACHT-LRR domains and does not bind oxidized TRX1, and it is unclear if it also detects reductive stress. In addition, it is not yet known whether reductive stress, protein folding, and XP peptide accumulation are all in some way directly related (Figure S1B).²⁷

Here, we wanted to identify small-molecule inducers of reductive stress and evaluate their impact on NLRP1 and CARD8 inflammasome activation. We discovered a panel of related radical-trapping antioxidants, and in particular JSH-23, that induce reductive stress, accelerate NT degradation of both NLRP1 and CARD8, and synergize with VbP to induce more pyroptosis. Moreover, we found that reductive stress and XP peptide accumulation together activate both NLRP1 and CARD8 in the absence of VbP. Overall, this work not

only establishes chemical probes that induce intracellular reductive stress but also reveals that both NLRP1 and CARD8 detect reductive stress.

RESULTS

Ferroptosis inhibitors synergize with VbP

We first wanted to assess the impact of antioxidants on NLRP1 and CARD8 inflammasome activation. We initially tested varying doses of a small panel of commonly used antioxidants on VbP-induced pyroptosis in mouse RAW 264.7 macrophages (NLRP1B dependent) and in human THP-1 and MV4;11 cell lines (CARD8 dependent) using CellTiter-Glo (CTG; which measures ATP levels as a proxy for cell viability).^{21,28} MeBs, which synergizes with VbP to induce more pyroptosis in these cell lines, was used as a positive control in this experiment.^{8,26} Consistent with our previous results,²⁷ we found that dithiothreitol (DTT), N-acetyl cysteine (NAC), reduced L-glutathione (GSH), and trolox did not synergize with VbP to induce more NLRP1 or CARD8 activation in this assay (Figures 1A, 1B, and S2A). Intriguingly, we observed that ferrostatin-1 (Fer-1), a lipophilic antioxidant that blocks an iron-dependent form of cell death called ferroptosis,²⁹ unlike other commonly used antioxidants, appeared to slightly synergize with VbP in RAW 264.7 and MV4;11 cells at a high (40 μ M) concentration (Figures 1A, 1B, and S2A). Consistent with these results, we found that Fer-1, like MeBs and unlike NAC, also increased VbP-induced lactate dehydrogenase (LDH) release and gasdermin D (GSDMD) cleavage, two hallmarks of pyroptosis, in these cells (Figures 1C and S2B). It should be noted that VbP and high concentrations (0.5 mM) of DTT induced slightly more GSDMD cleavage than VbP alone (Figures S2C–S2E). However, these high doses of DTT also activated the unfolded protein response (UPR) in the endoplasmic reticulum (ER) as evidenced by GRP78/BiP induction (Figures S2C–S2E). As UPR activation also accelerates NT degradation,²⁶ we cannot unambiguously ascribe this synergy to the induction of reductive stress in the cytosol. Regardless, these data suggested that Fer-1 might synergize with VbP by inducing such reductive stress, although this synergistic activity was modest and only observed at high doses.

We reasoned that other ferroptosis inhibitors might synergize with VbP more potently than Fer-1. Fortunately, a recent study identified dozens of ferroptosis-suppressing small molecules,³⁰ and we next tested these compounds for their impact on VbP-induced pyroptosis. Notably, we identified several, including JSH-23, AZD3463, SKI II, and WZ3146 (Figures 1D, 1E, and S2F), that dramatically synergized with VbP to induce more cell death in MV4;11 cells as measured by CTG. Of these, JSH-23 appeared to have the most synergistic activity. We confirmed that JSH-23 was non-toxic on its own up to 10 μ M after 6 h in both MV4;11 and RAW 264.7 cells but substantially increased VbP-induced death in both cell types as measured by propidium iodide (PI) uptake (Figure 1F), CTG, and CytoTox-Fluor (CTF; which measures extracellular protease activity after membrane permeabilization) assays (Figure 1G). Similar results were observed with SKI II, WZ3146, and AZD3463 in RAW 264.7 cells as well (Figure S2G). Notably, we found that JSH-23, unlike Fer-1 (Figures 1A and 1B), induced synergistic cell death with VbP in THP-1 cells (Figures S2H and S2I). Moreover, JSH-23, unlike DTT, did not activate the UPR (Figure

S2J). Collectively, these data strongly suggest that several ferroptosis inhibitors, and in particular JSH-23, profoundly enhance VbP-induced cell death.

We next wanted to confirm that these ferroptosis-suppressing small molecules were indeed inducing more pyroptosis and not some other form of cell death. Consistent with amplified pyroptotic cell death, we found that JSH-23, SKI II, AZD3463, WZ3146, and Fer-1 all increased VbP-induced LDH release and GSDMD cleavage in MV4;11 and RAW 264.7 cells (Figures 2A and 2B). Notably, JSH-23 also induced more LDH release and GSDMD cleavage with VbP in primary human resting T cells (which are CARD8 dependent),^{31,32} primary human peripheral blood mononuclear cells (PBMCs), and peripheral blood CD19⁺ B cells (Figures 2C–2E). It should be noted that cleavage of the inflammatory cytokines interleukin-1 β and -18 (IL-1 β /18), like LDH release and GSDMD cleavage, is typically considered to be a hallmark of pyroptotic cell death. However, inflammasomes that do not use the apoptosis-associated speck-like protein containing a CARD (ASC) adapter protein to bridge to CASP1, which include the CARD8 inflammasome and the NLRP1B inflammasome in RAW 264.7 cells (these cells lack ASC), do not appreciably cleave these cytokines.³³ In addition, although ASC-independent inflammasomes do induce the cleavage of pro-caspase-1 into its active form, the extent of processing is minimal and not typically observed by immunoblotting.³³ Thus, we did not evaluate cytokine or pro-caspase-1 cleavage in MV4;11, RAW 264.7, or resting T cells. In contrast to these cells, VbP activates the ASC-dependent human NLRP1 inflammasome in N/TERT-1 keratinocytes, which results in pronounced inflammatory cytokine cleavage.⁹ We found that JSH-23 increased VbP-induced LDH release as well as GSDMD, IL-1 β , and IL-18 cleavage in N/TERT-1 keratinocytes (Figure 2F), further indicating that JSH-23 is indeed triggering synergistic pyroptosis.

We next sought to show that this pyroptotic cell death was due to the activation of NLRP1 and CARD8 inflammasomes. Indeed, we found that *CARD8*^{-/-} and *CASP1*^{-/-} MV4;11 (Figures 2G, S3A, and S3B); *CARD8*^{-/-} and *CASP1*^{-/-} THP-1 cells (Figures S3C and S3D); *Nlrp1b*^{-/-} and *Casp1*^{-/-} RAW 264.7 cells (Figures 2H and S3E); and *NLRP1*^{-/-} N/TERT-1 keratinocytes (Figures S3F and S3G) were completely resistant to the combination of VbP and these ferroptosis inhibitors. The proteasome inhibitor bortezomib and caspase-1 inhibitor VX-765 block NLRP1- and CARD8-dependent cell death by inhibiting NT fragment degradation and GSDMD cleavage, respectively. Again consistent with NLRP1 and CARD8 activation, both bortezomib and VX-765 blocked VbP + JSH-23-induced cell death in MV4;11, RAW 264.7, and THP-1 cells (Figures 2G, 2H, and S3D). Thus, these ferroptosis-suppressing small molecules synergize with VbP to trigger more robust activation of the NLRP1 and CARD8 inflammasomes.

We wanted to determine if JSH-23 synergy was specific to VbP-induced NLRP1 and CARD8 activation or if it increased pyroptosis induced by other inflammasome activators. Notably, anthrax lethal toxin (LT) directly cleaves the mouse NLRP1B (allele 1) protein, inducing the N-end rule-mediated degradation of the NT fragment. We found that JSH-23, if anything, slightly suppressed LT-induced pyroptosis (Figure S3H). In addition, we found that JSH-23 had no impact on lipopolysaccharide (LPS) + nigericin-induced NLRP3 activation in THP-1 cells (Figure S3I), nor on LPS + nigericin-induced NLRP3 activation

or flagellin-induced NAIP/NLRC4 activation in RAW 264.7 cells stably expressing ASC (RAW 264.7^{ASC}) (Figure S3J). Thus, JSH-23 does not generally lead to greater inflammasome activation, but its effect appears specific to the VbP-induced pathway.

JSH-23 accelerates NT degradation

We next wanted to investigate if JSH-23 increased inflammasome activation by either accelerating NT degradation or destabilizing the DPP8/9 ternary complexes (Figure S1B). We previously generated *DPP8/9*^{-/-} THP-1 cells, which lack these repressive complexes and are completely resistant to VbP.²⁰ We found that JSH-23 induced additional lytic cell death and GSDMD cleavage in these cells (Figures 3A and 3B), which was blocked by the proteasome inhibitor bortezomib (Figure S4A). In addition, we found that JSH-23 treatment of *CASP1*^{-/-} MV4;11 cells (knockout cells were used to prevent any pyroptotic cell death) induced a slight reduction in the amount of CARD8^{NT} fragment by immunoblotting (Figures 3C and S4B). It should be noted that only a small amount of the free CARD8^{CT} is required to induce pyroptosis,^{7,8,34} and therefore even slight degradation is likely physiologically important. Similarly, we only found that JSH-23 induces slight degradation of NLRP1 in N/TERT-1 keratinocytes as evaluated by immunoblotting (Figure S4C). Regardless, these degradation results, coupled with the proteasome blockade and *DPP8/9* knockout data above, collectively indicate that JSH-23 induces synergistic pyroptosis, at least in part, by accelerating NT degradation.

Even so, we reasoned that it remained possible that JSH-23 might also destabilize the DPP8/9 ternary complex in wild-type cells. We therefore next tested JSH-23 in an assay we previously developed to assess ternary complex disruption in cells (Figure 3D).¹² This assay relies on the degron tag system, in which the small molecule dTAG-13 induces the rapid degradation of proteins fused to degron tags (dTAGs).³⁵ Here, we appended a dTAG to the N terminus of the CARD8 ZU5-UPA-CARD region to generate a dTAG-13-activatable fusion protein (dTAG-CARD8^{ZUC}; Figure 3D) and transiently expressed this fusion protein in HEK293T cells stably expressing GSDMD and CASP1 (HEK293T^{CASP1+GSDMD}). Notably, dTAG-CARD8^{ZUC} is insensitive to VbP because it lacks the NT disordered region required for DPP8/9 inhibitor-induced NT degradation.^{12,34} As expected, dTAG-13, but not VbP, JSH-23, or VbP + JSH-23, treatment triggered dTAG-CARD8^{ZUC} degradation and induced pyroptosis in these cells (Figure 3E, lane 3). Importantly, co-expression of an autoproteolysis-defective S297A mutant CARD8 FIIND domain (FIIND^{SA}) blocked this pyroptosis by sequestering the dTAG13-generated free CARD8^{CT} in a repressive ternary complex (Figures 3D and 3E, lane 4 versus 3). We found that VbP destabilized this repressive complex and restored LDH release and GSDMD cleavage (Figure 3E, lane 6 versus 4), but JSH-23 had no impact on this assay (Figure 3E, lane 8 versus 4). Thus, JSH-23 does not destabilize the DPP8/9 ternary complex in this experiment.

We instead predicted that JSH-23 acts primarily (and perhaps solely) by accelerating NT fragment degradation, even if it was barely observable by immunoblotting (Figures 3C and S4C). Moreover, we speculated that JSH-23 does not induce pyroptosis on its own (in the absence of VbP) because the released CT fragments are effectively quenched by the DPP8/9 ternary complex (Figure S4D). To test this idea, we next introduced a construct

encoding a doxycycline (DOX)-inducible E274R mutant CARD8 protein into *CARD8*^{-/-} THP-1 cells. Importantly, the FL CARD8 E274R protein cannot bind to DPP8/9, and therefore any released free CT fragments are not sequestered in the ternary complex but instead form inflammasomes¹² (Figure S4D). Indeed, DOX treatment induced spontaneous pyroptosis in these cells due to the generation of free CARD8^{CT} fragments during homeostatic protein turnover (Figure 3F). Consistent with our hypothesis, we found that JSH-23 induced additional pyroptosis in CARD8 E274R-expressing cells, and bortezomib completely blocked this cell death. Similarly, we found that JSH-23 induced more pyroptosis in *CARD8*^{-/-} THP-1 cells ectopically expressing NLRP1 P1214R, which also has attenuated binding to DPP9 (Figure S4E).⁹ These data demonstrate that JSH-23 alone induces a danger signal that accelerates the degradation of the NT fragments but that the DPP8/9 ternary complex prevents the resulting free CT fragments from inducing pyroptosis. VbP synergizes with JSH-23 because it prevents DPP8/9 from sequestering these newly released CT fragments.

Synergistic compounds are radical-trapping antioxidants

Our next objective was to identify the danger state induced by the ferroptosis inhibitors. Before exploring their antioxidant activities, we first confirmed that JSH-23 and SKI II do not inhibit recombinant DPP9 (Figure 4A) and that JSH-23, SKI II, AZD3463, and WZ3146 do not inhibit DPP8/9 activity in living HEK293T cells (Figure 4B). 8j is a selective DPP8/9 inhibitor and was used as a control in this experiment.³⁶ As mentioned previously, non-selective inhibitors of APs, including MeBs, synergize with VbP to induce more NLRP1 and CARD8 inflammasome activation.^{8,26} We also confirmed that the ferroptosis inhibitors, unlike MeBs, do not block AP activity in cells (Figure 4C). Lastly, we showed that these compounds, unlike the proteasome inhibitors bortezomib and MG132, do not impact overall proteasome activity in cells (Figure 4D). Thus, these compounds do not interfere with any of the known pathways that regulate NLRP1 and CARD8 inflammasome activation.

We next sought to verify that these compounds indeed inhibited ferroptosis. The small molecule RSL3 induces ferroptosis by inhibiting glutathione peroxidase 4 (GPX4), thereby causing the accumulation of lipid peroxides and cell death.³⁷ We found that all five of the reported ferroptosis inhibitors completely blocked RSL3-induced death in RAW 264.7 cells (Figures 4E, 4F, S5A, and S5B). In contrast, NAC only partially blocked ferroptosis, even at high (millimolar) concentrations, and the caspase-1 inhibitor VX-765 had no impact in this experiment. Fer-1 and JSH-23 were the most potent ferroptosis inhibitors, blocking cell death at low nanomolar concentrations (<100 nM), whereas SKI II and WZ3146 required low micromolar concentrations to effectively block cell death. Thus, these compounds all share the ability to inhibit ferroptosis. Notably, their ferroptosis-blocking activities generally correlate with their pyroptosis-inducing activities, with the exception that Fer-1 is far more effective in suppressing ferroptosis.

We next wondered if the pyroptosis-inducing abilities of these compounds might correlate more strongly with their abilities to quench free radicals. As such, we next tested the ability of these compounds to directly scavenge free radicals *in vitro* using the cell-free 2,2-diphenyl-1-picrylhydrazyl (DPPH) assay. JSH-23 and Fer-1, and to a lesser extent

AZD3463, SKI II, and WZ3146, indeed scavenged free radicals (Figure 4G). However, we found that NAC and trolox, which do not induce synergistic pyroptosis, also had potent activity in this assay. Thus, the synergistic compounds all scavenge radicals *in vitro*, but this activity alone does not predict their impact on NT degradation in cells. As expected, VbP and MeBs had no impact on DPPH absorbance, consistent with their distinct mechanisms of action (Figure 4G).

We next wanted to assess the impact of these compounds in cell-based antioxidant activity assays. The cell-permeable 2',7'-dichlorodihydrofluorescein diacetate dye (DCFDA), which fluoresces upon oxidation, is commonly used to measure intracellular ROS. We found that JSH-23 and SKI II slowed DCFDA oxidation but so did NAC, DTT, and trolox (Figures 4H and S5C). Moreover, AZD3463 and WZ3146 did not show activity in this assay. Thus, DCFDA oxidation further supports the idea that JSH-23 is an antioxidant but also that this assay likely does not measure the form of intracellular ROS that suppresses pyroptosis. We next tested the impact of these compounds on the oxidation of the C11 BODIPY probe, which acts as a sensor of lipid peroxidation in cells. We found that JSH-23, AZD3463, SKI II, and WZ3146, but not Fer-1, slowed the basal oxidation of this probe in cells (Figures 4I and S5D). Moreover, we found that these compounds, except WZ3146, substantially suppressed RSL3-induced oxidation of this probe. These data further support the idea that the synergistic compounds are all antioxidants, and their activities in this assay, as in the ferroptosis blockade assay, generally correlate with their pyroptosis-inducing abilities. Overall, these results confirm that JSH-23 and the other ferroptosis inhibitors act as radical-trapping antioxidants (RTAs), even if these commonly used assays do not precisely measure the intracellular ROS that regulates inflammasome activation.

Structure-activity relationship of the RTAs

JSH-23, SKI II, WZ3146, AZD3463, and Fer-1 all have aromatic secondary amines that can potentially scavenge free radicals (Figure S6A, colored red)^{38–40} but are otherwise not structurally related. We noticed that several additional hits from the primary screen similarly had such secondary aromatic amines (WZ4002, WZ8040, WHI-P154, and RAF265), but some other hits did not (MC1568, bazedoxifene) (Figures 1D, blue arrows, and S6A). Interestingly, only the compounds with the secondary aromatic amines exhibited synergistic pyroptotic activity in confirmation assays in MV4;11 cells (Figure S6B). To directly investigate the importance of this moiety, we next purchased analogs of JSH-23 itself (Figure 5A). Notably, compound 1, which has a second phenyl group directly attached to the secondary amine, retained synergistic activity in CTG assays in both MV4;11 and RAW 264.7 cells (Figures 5B and 5C). However, compound 2, which is identical to 1 but without a secondary amine, lacked all activity. The primary amine was also critical, as diarylamine (compound 7) was inactive. As expected, compounds 6 and 11, which have substituents on the secondary amine similar to JSH-23, were also active. Lastly, the electronics of the aromatic ring of 6 appeared to be critical, as the replacement of the electron-donating methyl group with an electron-withdrawing cyano group (compound 4) ablated all activity. We confirmed that the CTG results indeed reported pyroptotic cell death, as the active compounds increased VbP-induced PI uptake in MV4;11 cells (Figure 5D) as well as LDH release and GSDMD cleavage in both MV4;11 cells and RAW 264.7 cells (Figures 5E

and S6C). As expected, this cell death was completely blocked by bortezomib and VX-765 (Figures S6D and S6E).

Not surprisingly, the synergistic compounds, but not the inactive compound 2, appeared to have mechanisms of action like JSH-23. For example, the synergistic compounds induced additional bortezomib-sensitive pyroptosis in *CARD8*^{-/-} THP-1 cells ectopically expressing the DPP9-non-binding mutant CARD8 E274R (Figures 5F and 5G), induced some visible CARD8^{NT} depletion by immunoblotting (Figures 5H and S6F), trapped free radicals in the DPPH assay (Figure S6G), and acted as antioxidants in the cell-based C11 BODIPY and DCFDA assays (Figures 5I and S6H). Overall, these data show that the conjugated amines of JSH-23 are critical for its activity as these groups likely trap specific ROS species inside cells, induce reductive stress, and accelerate NT degradation.

AP inhibitors and RTAs trigger CARD8 activation

As mentioned above, we recently discovered that the AP inhibitor MeBs synergizes with VbP to induce more NLRP1 and CARD8 inflammasome activation,⁸ similar to the RTAs studied here. However, MeBs does not trap free radicals (Figure 4G), but instead induces the accumulation of intracellular oligopeptides that accelerate NT degradation.²⁶ Thus, JSH-23 and MeBs have distinct mechanisms of action. Accordingly, we hypothesized that the combination of MeBs and JSH-23 might induce sufficient NT degradation and CT release to overcome the repressive DPP8/9 ternary complex even in the absence of VbP. To test this premise, we next treated MV4;11 cells with JSH-23 and increasing doses of MeBs. Excitingly, we observed that this drug combination stimulated pyroptosis in wild-type (WT), but not *CASPI*^{-/-}, MV4;11 cells (Figures 6A, 6B, and S7A). As expected, JSH-23 + MeBs induced degradation of the CARD8^{NT} fragment (Figure 6C), although the additional impact of MeBs on JSH-23-induced degradation is difficult to observe by immunoblotting. Nevertheless, this degradation was critical, as JSH-23 + MeBs-triggered pyroptosis was blocked by VX-765 and bortezomib (Figure 6D). We similarly observed that JSH-23 + MeBs induced inflammasome activation in CARD8-dependent THP-1 cells and OCI-AML2 cells (Figures 6E and S7B). We found that this drug combination did not appear to impact DPP8/9 activity nor destabilize the CARD8-DPP8/9 ternary complex in cells (Figures 6F and S7C) but did increase the activation of CARD8 E274R higher than either drug alone (Figure 6G). Overall, these results indicate the AP inhibitors and RTAs together induce sufficient NT degradation to activate the CARD8 inflammasome. Even though we do not see evidence of CARD8-DPP8/9 ternary complex destabilization, we should note that it remains possible that this drug combination might also induce the accumulation of some peptides (or trigger some as-yet-unknown perturbation) that weakens this checkpoint in a way that is difficult to directly observe.²⁶

In contrast to CARD8, we found that MeBs + JSH-23 did not activate mouse NLRP1B (allele 1) in RAW 264.7 cells (Figure 6H), mouse NLRP1A and/or NLRP1B (allele 2) in C57BL/6 bone-marrow-derived macrophages (BMDMs; Figure 6I), or the human NLRP1 inflammasome N/TERT-1 keratinocytes (Figure 6J). To confirm that the inability of JSH-23 + MeBs to activate NLRP1 was due to NLRP1 itself and not the distinct cell types, we next ectopically expressed CARD8 or NLRP1 in *CARD8*^{-/-} THP-1 cells. As expected, VbP

alone or in combination with MeBs or JSH-23 induced GSDMD cleavage in both cell types, but JSH-23 + MeBs only triggered GSDMD cleavage (albeit modestly) in cells expressing CARD8 (Figures 6K and 6L). Similarly, compounds 1, 6, and 11 in combination with MeBs also induced CARD8 inflammasome activation in MV4;11 cells but not NLRP1B inflammasome activation in RAW 264.7 cells (Figures S7D–S7F). Collectively, these data indicate that these combinations do not induce sufficient NT degradation and/or ternary complex destabilization to activate NLRP1. These results are consistent with the idea that NLRP1 has a higher activation threshold than CARD8, as discussed below.^{10,12,25}

XP peptides and RTAs activate NLRP1 and CARD8

We recently described a small molecule called CQ31 that inhibits the APs PEPD and XPNPEP1 and thereby causes the intracellular accumulation of XP peptides. Interestingly, CQ31 alone, like the MeBs + JSH-23 combination, activates the human CARD8, but not the human NLRP1, inflammasome.²⁵ NLRP1, unlike CARD8, directly interacts with the DPP8/9 active site in the ternary complex,^{10,12} and we hypothesized that the CQ31-accumulated peptides did not sufficiently destabilize the NLRP1-DPP9 interaction to trigger inflammasome activation, at least in the absence of a stimulus that potently accelerates NT degradation.

We next wondered if the combination of CQ31 and JSH-23 together would induce pyroptosis. As expected, we found JSH-23 synergized with CQ31 to induce more CARD8-dependent pyroptosis in MV4;11 cells (Figure 7A). Notably, CQ31 + JSH-23 induced more cell death than VbP alone, CQ31 alone, or CQ31 + MeBs at this time point. Intriguingly, we found that the combination of JSH-23 + CQ31 also slightly activated the human NLRP1 inflammasome in N/TERT-1 keratinocytes, and the triple combination of JSH-23 + MeBs + CQ31 caused substantial NLRP1 activation (Figures 7A and S7G). However, this triple-drug cocktail was still unable to activate the mouse NLRP1B inflammasome in RAW 264.7 cells (Figure S7H), consistent with previous data that show that the mouse NLRP1 inflammasome has an especially high activation threshold.^{19,41,42} Regardless, these data collectively indicate that human CARD8 and NLRP1 are activated by the same danger signals, but NLRP1 has a higher activation threshold that requires the simultaneous occurrence of several key inputs (Figures 7C and 7D).

DISCUSSION

We recently discovered that the oxidized, but not the reduced, form of TRX1 binds to and represses NLRP1.²⁷ As such, we predicted that reductive stress would abrogate this interaction and lead to inflammasome activation. However, no agents were known that induce reductive stress to test this hypothesis. Here, we identified and characterized several RTAs, and in particular JSH-23, that induce reductive stress. To the best of our knowledge, these are the strongest known inducers of such reductive stress, and we predict they will gain widespread use to study this biological perturbation. Here, we used these probes to discover that reductive stress induces the degradation of NT fragments of both NLRP1 and CARD8, thereby releasing the CT fragments from autoinhibition. As CARD8 does not bind

TRX1, these data indicate that reductive stress is monitored in at least two distinct ways, as discussed below.

The mechanisms that control the acceleration of NT degradation are starting to come into focus. We recently discovered that MeBs (and perhaps, but to a far lesser extent, VbP) induces the accumulation of proteasome-derived peptides and that these peptides interfere with the folding of the NT domains, potentially by inhibiting chaperones.²⁶ These misfolded domains are then destroyed by the ubiquitin-independent core 20S proteasome.⁴³ We speculate that reductive stress similarly interferes with protein folding. Indeed, oxidative power is critical for protein folding in the ER⁴⁴; it seems possible that oxidative power plays a similar, but as-yet-unknown, role in the folding of cytosolic proteins, including NLRP1's and CARD8's NT fragments. In addition, we recently discovered that oxidized TRX1 stabilizes NLRP1 NT's structure,²⁷ which we now speculate serves as a "checkpoint" to ensure misfolding is indeed associated with reductive stress. Whether a redox-sensitive protein similarly regulates the folding of the CARD8 NT remains to be determined. In either case, future studies are needed not only to fully elucidate how reductive stress causes inflammasome activation but also how it impacts proteostasis more generally.

Notably, our work here further confirms the importance of cytosolic ROS for the maintenance of homeostasis,⁴⁵ but many mysteries regarding this ROS remain unanswered. For example, the identity, source, and regulation of the ROS that suppresses inflammasome activation are unknown, and why amine-based antioxidants (e.g., JSH-23), and not thiol-based antioxidants (e.g., NAC), effectively suppress this ROS has not been established. Furthermore, it is not yet clear what intracellular redox potential constitutes reductive stress, and how cells without inflammasomes respond to this perturbation. On that note, FNIP1 and CUL2^{FEM1B} were recently discovered as core components of the reductive stress response to mitochondrial inactivity.⁴⁶ Projecting forward, it will be important to determine the relationships between cellular redox potential, FNIP1-CUL2^{FEM1B} signaling, TRX1 oxidation, and inflammasome activation.

Overall, our data here, coupled with our other recent studies,^{25,26} have now revealed that NLRP1 and CARD8 both detect at least two distinct danger signals: reductive stress and XP peptide accumulation. We speculate that these two signals are intimately related and together indicate that the cell is experiencing a specific intracellular "damage state." Lastly, we should note that, even though chemical probes have proved exceptionally useful in deconvoluting these danger signals, future studies are needed to understand how pathogens (and potentially other homeostasis-altering perturbations) induce reductive stress and XP peptide accumulation. Ultimately, we expect that these investigations will not only reveal key aspects of innate immunity but will also uncover the mechanisms that regulate some of the most primordial processes in all of biology.

Limitations of this study

We acknowledge that this study has several limitations. First, we were unable to directly measure the reductive stress associated with NLRP1/CARD8 inflammasome activation in cells using currently available redox assays, hampering our ability to precisely identify this cell state. Second, although it appeared that JSH-23 induced NLRP1/CARD8 activation via

NT degradation and not DPP8/9 ternary complex destabilization, we cannot be certain that our ternary complex assay (i.e., the dTAG assay) was sufficiently sensitive to rule out small disruptive effects. Third, JSH-23 and the related RTAs, like all small molecules, may have off targets that in some way impact cells in addition to reductive stress. Future studies will be needed to develop additional assays that monitor intracellular redox potential, create more sensitive approaches to evaluate DPP8/9 ternary complex destabilization, and identify distinct stimuli (including pathogens) in addition to RTAs that induce reductive stress.

STAR★METHODS

RESOURCE AVAILABILITY

Lead contact—Further information and requests for resources and reagents should be directed to and will be fulfilled by the lead contact, Daniel A. Bachovchin (bachovcd@mskcc.org).

Material availability—Materials generated in this study are available from the lead contact upon reasonable request.

Data and code availability

- Unprocessed data underlying the display items in the manuscript, related to figures, are available from the lead contact upon request.
- This paper does not report original code.
- Any additional information required to analyze the data reported in this paper is available from the lead contact upon request.

EXPERIMENTAL MODEL AND SUBJECT DETAILS

HEK 293T, THP-1, RAW 264.7, and Primary Peripheral Blood Mononuclear cells were purchased from ATCC. OCI-AML2 and MV4; 11 cells were purchased from DSMZ. Naive CD3⁺ human T cells were purchased from HemaCare (Lot #21068415). Human Peripheral Blood CD19⁺ B Cells were purchased from Stemcell Technologies (Cat # 70033). N/TERT-1 cells were a gift from the Rheinwald Lab.⁴⁷ HEK 293T and RAW 264.7 cells were grown in Dulbecco's Modified Eagle's Medium (DMEM) with L-glutamine and 10% fetal bovine serum (FBS). Naive human CD3 T cells, Primary Peripheral Blood Mononuclear Cells, human Peripheral Blood CD19⁺ B Cells, THP-1, MV4; 11, and OCI-AML2 cells were grown in Roswell Park Memorial Institute (RPMI) medium 1640 with L-glutamine and 10% FBS. N/TERT-1 cells were grown in Keratinocyte serum-free medium (KSFM) supplemented with 1X penicillin/streptomycin, bovine pituitary extract (25 µg/mL) and epidermal growth factor (EGF) (0.2 ng/mL). All cells were grown at 37°C in a 5% CO₂ atmosphere incubator. Cell lines were regularly tested for mycoplasma using the MycoAlert Mycoplasma Detection Kit (Lonza). *CARD8*^{-/-}, *DPP8*^{-/-}/*DPP9*^{-/-}, and *CASPI*^{-/-} THP-1 cells, *CASPI*^{-/-} and *Nlrp1b*^{-/-} RAW 264.7 cells, *CARD8*^{-/-}, and *CASPI*^{-/-} MV4; 11, *NLRP1*^{-/-} N/TERT-1 cells were generated as previously described.^{20,21,27} Doxycycline (DOX)-inducible *CARD8* and *NLRP1* WT and mutant knock-in *CARD8*^{-/-} THP-1 were generated as previously described.^{10,12}

METHOD DETAILS

CRISPR/Cas9 gene editing—*DPP8/9*, *CARD8*, and *CASP1* knockout THP-1 cell lines and all HEK293T, RAW 264.7, N/TERT-1, and MV4; 11 knockout cell lines were generated as previously described.^{12,20,21,27} Briefly, 5×10^5 HEK 293T cells stably expressing Cas9 were seeded in 6-well tissue culture dishes in 2 mL of media per well. The next day cells were transfected according to the manufacturer's instructions (FuGENE HD, Promega) with 2 μ g of the sgRNA plasmid(s). After 48 h, cells were transferred to a 10 cm tissue culture dish and selected with puromycin (1 μ g/mL) until the control cells were all dead. Single cell clones were isolated by serial dilution and confirmed by Western blot or sequencing, as indicated. To generate knockouts in RAW 264.7, MV4; 11 and THP-1 cells, 1.5×10^6 cells stably expressing Cas921 were infected with lentivirus containing sgRNA plasmids. After 48 h, cells were selected with puromycin (1 μ g/mL) or hygromycin (100 μ g/mL). Single cell clones were isolated by serial dilution and confirmed by Western blotting. *NLRP1* knockout N/TERT-1 keratinocytes were prepared by using the Neon Transfection System (ThermoFisher Scientific) following the manufacturer's recommendations to deliver Cas9 ribonucleoprotein complexes containing an Alt-R CRISPR-Cas9 sgRNA and recombinant Cas9 (IDT). Briefly, sgRNA complexes were prepared by combining pre-designed Alt-R CRISPR-Cas9 crRNA (*NLRP1*: 5' - CTGGATCCATGAATTGCCGG-3') with Alt-R CRISPR-Cas9 tracrRNA to 44 μ M and annealing by heating to 95°C for 5 min followed by gradual cooling to ambient temperature over 30 min. To form the RNP complexes sgRNA samples and recombinant Alt-R Cas9 enzyme were combined and incubated for 20 min.

Stable cell line generation—Cells stably expressing indicated protein constructs were generated by infection with lentivirus containing the desired plasmids. Briefly, the lentivirus was produced by transfecting 70% confluent HEK 293T cells with the desired plasmid along with psPAX2 and pMD2.G following the manufacturer's instructions (FuGENE HD, Promega). The virus-containing medium was collected 48 h after transfection, passed through a 0.45 μ m filter, and concentrated by PEG precipitation (Abcam). THP-1 cells were infected with the prepared lentivirus by centrifuging at $1000 \times g$ for 1 h. After 48 h of incubation, cells were selected with an appropriate antibiotic.

Transient transfections—HEK 293T cells were plated in 6-well tissue culture plates at 5.0×10^5 cells/well in DMEM. The next day, the indicated plasmids were mixed with an empty vector to a total of 2.0 μ g DNA in 125 μ L Opti-MEM and transfected using FuGENE HD (Promega) according to the manufacturer's protocol.

Cloning—Plasmids for *CARD8* WT and variants, *CASP1*, *GSDMD*, *NLRP1* WT and variants, dTAG-CARD8^{ZUC} were cloned as described previously.^{10,12,21} Briefly, DNA sequences encoding the genes were purchased from GenScript, amplified by polymerase chain reaction (PCR), shuttled into the Gateway cloning system (ThermoFisher Scientific) using pDONR221 and pLEX307 vectors originating from pLEX307 (Addgene #41392). sgRNAs were designed using the Broad Institute's web portal⁴⁸ (<http://www.broadinstitute.org/rnai/public/analysis-tools/sgrna-design>) and cloned into the lentiGuide-puro vector (Addgene #52963) as described previously (Sanjana et al., 2014). The sgRNA sequences used are described in the STAR Methods table.

CellTiter-Glo and CytoTox-Fluor cytotoxicity assays. Cells were plated (2,000 cells per well) in white, 384-well clear-bottom plates (Corning) using an EL406 Microplate Washer/Dispenser (BioTek) in 25 μ L final volume of the cell culture medium. Adherent cells were plated 12 h before treatment. To the cell plates were added compounds at different concentrations using a pintoole (CyBio) and the plates were allowed to incubate for 1 h in the incubator before adding VbP (10 μ M). After incubation for indicated times, CytoTox-Fluor reagent (Promega, G9262) was added according to the manufacturer's protocol. The assay plates were then incubated for another 30 min before fluorescence was recorded using a Cytation 5 Cell Imaging Multi-Mode Reader (BioTek). Next, CellTiter-Glo reagent (Promega, G7573) was subsequently added to the assay plates following the manufacturer's protocol. Assay plates were shaken on an orbital shaker for 2 min and incubated at 25°C for 10 min. Luminescence was then read using a Cytation 5 Cell Imaging Multi-Mode Reader (BioTek).

Excess over Bliss (EoB) calculation. EoB score is used to measure the combined effect of compound and VbP.^{49,50} EoB > 0 indicates the compound synergizes with VbP-induced cell death, EoB < 0 indicates the compound blocks VbP-induced cell death, and it was calculated using the following equations:

$$EoB = E_{observed} - E_{predicted}$$

Where $E_{observed}$ is the observed cell death for the treatment of compound + VbP and was calculated by subtracting the observed viability based on CTG assay from 100. $E_{predicted}$ was calculated based on the following equation:

$$E_{predicted} = Y_{compound} + Y_{VbP} - Y_{compound} * Y_{VbP}$$

where $Y_{compound}$ is the observed cell death with compound alone at indicated dose and Y_{VbP} is the observed cell death with VbP (10 μ M) alone. $Y_{compound}$ and Y_{VbP} are calculated by subtracting the observed viability for compound and VbP based on CTG assay from 100, respectively. All compounds were tested in triplicate at indicated doses.

Propidium iodide uptake analysis— 2×10^4 MV4; 11 or THP-1 cells were plated in 384-well, black, clear-bottom plates (Corning) in 40 μ L of RPMI medium. RAW 264.7 cells were plated 12 h before treatment. Cells were then treated as indicated and 40 μ L propidium iodide (PI) at 20 μ M was added to each well. PI fluorescence was measured at Ex/Em: 535/617 nm at 37°C every 5 min using Cytation 5 Cell Imaging Multi-Mode Reader (BioTek). The obtained measurements were baseline corrected to DMSO at each time point and was presented as $F_{treatment} - F_{DMSO}$. $F_{treatment}$, Fluorescence measurement for compound treatment at time t; F_{DMSO} , fluorescence measurement for DMSO control at time t.

LDH cytotoxicity assays—MV4; 11, THP-1, OCI-AML2, RAW 264.7, and RAW 264.7^{ASC} cells were plated in 12-well tissue culture plates at 5×10^5 cells/well, Naive human CD3 T cells were plated in 12-well tissue culture plates at 2×10^6 cells/well.

N/TERT-1 keratinocytes were seeded at 2×10^5 cells/well (in 2 mL medium) in 6-well tissue culture plates. RAW 264.7, and RAW 264.7^{ASC} cells were incubated overnight before treatment. N/TERT-1 keratinocytes were incubated for 48h before treatment. *CARD8*^{-/-} THP-1 cells containing a DOX-inducible CARD8 WT, NLRP1 WT, CARD8 E274R, or NLRP1 P1214R protein were seeded at 2.5×10^5 cells/well in 12-well tissue culture dishes. The cells were then pre-incubated with the indicated concentration of doxycycline for indicated times before compound treatment. For all cells, after treatment with indicated compounds for indicated times, supernatants were analyzed for LDH activity using the Pierce LDH Cytotoxicity Assay Kit (Life Technologies). LDH activity was quantified relative to a lysis control where cells were lysed by adding 8 μ L of a 9% Triton X-100 solution.

Ferroptosis assays—RAW 264.7 cells were plated (2,000 cells per well) in white, 384-well clear-bottom plates (Corning) manually in 25 μ L final volume of the cell culture medium. After overnight incubation, cell plates were allowed to pre-treat with compounds using a pintoole (CyBio) for 30 min in the incubator before adding RSL3 (0.25 μ M). After 4.5 h, cytotoxicity was assessed by CTF and CTG assay as mentioned in the CellTiter-Glo and CytoTox-Fluor cytotoxicity assays part.

DCFDA/H₂DCFDA cellular ROS assay—This assay was carried out using a cellular ROS kit (Abcam, Ab113851) according to the manufacturer's instructions. Briefly, 1 X ROS assay buffer was freshly prepared and DCFDA solution was diluted to 20 μ M with this newly prepared buffer. *CASP1*^{-/-} MV4; 11 or THP-1 cells were collected, washed with PBS, suspended in 20 μ M DCFDA solution (1 mL per million cells), and incubated for 30 min. Cells were then centrifuged, washed with PBS twice, suspended in corresponding cell culture medium (supplemented with 10% FBS) without phenol red, and plated (10,000 cells/well) in black, 384-well clear-bottom plates (Corning) manually in 25 μ L final volume before treated with compounds. Fluorescence was measured at Ex/Em: 485/535 nm recorded at 37°C every 5 min using Cytation 5 Cell Imaging Multi-Mode Reader (BioTek).

Cell-free 2,2-diphenyl-1-picrylhydrazyl (DPPH) assay—Freshly prepared DPPH solution in methanol (40 μ M) was plated on white, 384-well clear-bottom plates. Methanol was utilized as a background control. Compounds were added at different concentrations using a pintoole (CyBio) and the cell plate was sat in dark for 1 h before absorbance at 517 nm was recorded using Cytation 5 Cell Imaging Multi-Mode Reader (BioTek). All values were normalized to the background. Each condition was tested in triplicate.

C11 BODIPY 581/591 assay—*CASP1*^{-/-} MV4; 11 cells were seeded at 1×10^6 in a 6-well plate and treated for 2.5 h with the indicated compounds before staining with 5 μ M of C11 BODIPY 581/591 for an additional 30 min. Cells were subsequently collected, washed twice with FACS buffer (PBS with 2.5% FBS), and analyzed for the FITC and PE-CF594 fluorochromes using the Fortessa (BD Biosciences). Unstained, DAPI only, and C11 BODIPY 581/591 only technical controls were included to ensure proper gating. The gating pipeline starts by isolating the bulk cell population and excluding doublets, then choosing the population that was DAPI negative before plotting the histogram of cells

corresponding to the FITC fluorochrome. To note, the C11-BODIPY dye emits a green wavelength when oxidized.

AMC substrate assays—For recombinant enzyme assays, 25 μ L DPP9 enzyme solution (1.0 nM) was added to a 384-well, black, clear-bottom plate (Corning). Compounds at different concentrations were added using a pintoole (CyBio) and the enzyme plate was shaken at room temperature for 45 min, followed by Ala-Pro-AMC (25 μ M) substrate to initiate the reaction. For in-cell assays, 8.0×10^4 *CASP1*^{-/-} MV4; 11 or HEK 293T cells were seeded per well in a 96-well, black, clear-bottom plate (Corning) (overnight for HEK 293T cells) in OptiMEM and treated with compounds for 5 h, and then with Sitagliptin (1 μ M) to block DPP4 activity for 1h before substrate (Ala-Pro-AMC, 5 μ M; Ala-AMC, 100 μ M) was added to the media to initiate the reaction. AMC fluorescence (Ex/Em: 380/460 nm) was recorded at 25°C for 30–60 min. Cleavage rates are reported as the slope of the linear regression of AMC fluorescence vs. time data curve.

IL-1 β ELISA assays— 2×10^5 N/TERT-1 keratinocytes in 2 mL cell culture medium were plated on 6-well tissue culture plates and incubated for 48 h. Cells were then treated with compounds for the indicated time points before LDH release analysis. 200 μ L spent media sample were collected, centrifuged at 1000 g for 1 min, and the supernatants were utilized for IL-1 β quantification using the R&D Human IL-1 β quantikine ELISA kit according to the manufacturer's instructions.

Immunoblotting—Cells were washed $2 \times$ in PBS (pH = 7.4), resuspended in PBS, and lysed by sonication. Protein concentrations were determined and normalized using the DCA Protein Assay kit (Bio-Rad). To prepare supernatant western blotting samples of N/TERT-1 keratinocytes, spent media of each treatment were combined, centrifuged at 400 g for 3 min, and the supernatant was precipitated by addition of four sample volumes of acetone at -20°C overnight followed by centrifugation at 3000 g for 30 min at 4°C and decanting. Protein pellets were then suspended in 1X PBS and combined 1:1 with 2X sample loading buffer before heating to 97°C for 10 min.

Samples were run on NuPAGE 4 to 12%, Bis-Tris, 1.0 mM, Midi Protein Gel (Invitrogen) for 45–60 min at 175 V. Gels were transferred to nitrocellulose with the Trans-Blot Turbo Transfer System (BIO-RAD). Membranes were blocked with Intercept (TBS) Blocking Buffer (LI-COR) for 30 min at ambient temperature, before incubating with primary antibody overnight at 4°C . Blots were washed 3 times with TBST buffer before incubating with secondary antibody for 60 min at ambient temperature. Blots were washed 3 times, rinsed with water, and imaged via Odyssey CLx (LI-COR).

dTAG-CARD8 assay—HEK 293T cells stably expressing CASP1 and GSDMD were seeded at 1.5×10^5 cells per well in 12-well tissue culture dishes. After 48 h, the cells were transfected with plasmids encoding dTAG-CARD8-ZUC (0.5 μ g), CARD8 FIIND-S297A (0.3 μ g), and RFP (0.2 μ g) with FuGENE HD, according to the manufacturer's instructions (Promega). After 24 h, cells were treated with DMSO, dTAG13 (500 nM), and indicated compounds for 3 h prior to LDH release and immunoblot analyses.

QUANTIFICATION AND STATISTICAL ANALYSIS

Two-sided Student's *t* tests were used for significance testing unless stated otherwise. *p* values less than 0.05 were considered to be significant. Graphs and error bars represent means \pm SEM of three independent experiments unless stated otherwise. The investigators were not blinded in all experiments. All statistical analysis was performed using Microsoft Excel and GraphPad Prism 9.

Supplementary Material

Refer to Web version on PubMed Central for supplementary material.

ACKNOWLEDGMENTS

This work was supported by the NIH (R01 AI137168, R01 AI163170, and R01 CA266478 to D.A.B.; the MSKCC Core Grant P30 CA008748; and T32 GM115327-Tan to E.L.O.-H), Gabrielle's Angel Foundation (D.A.B.), Mr. William H. and Mrs. Alice Goodwin, the Commonwealth Foundation for Cancer Research, The Center for Experimental Therapeutics of Memorial Sloan Kettering Cancer Center (D.A.B.), and the Emerson Collective (D.A.B.).

REFERENCES

1. Broz P, and Dixit VM (2016). Inflammasomes: mechanism of assembly, regulation and signalling. *Nat. Rev. Immunol.* 16, 407–420. 10.1038/nri.2016.58. [PubMed: 27291964]
2. Taabazuig CY, Griswold AR, and Bachovchin DA (2020). The NLRP1 and CARD8 inflammasomes. *Immunol. Rev.* 297, 13–25. 10.1111/immr.12884. [PubMed: 32558991]
3. Bachovchin DA (2021). NLRP1: a jack of all trades, or a master of one? *Mol. Cell* 81, 423–425. 10.1016/j.molcel.2021.01.001. [PubMed: 33545058]
4. D'Osualdo A, Weichenberger CX, Wagner RN, Godzik A, Wooley J, and Reed JC (2011). CARD8 and NLRP1 undergo autoproteolytic processing through a ZU5-like domain. *PLoS One* 6, e27396. 10.1371/journal.pone.0027396. [PubMed: 22087307]
5. Finger JN, Lich JD, Dare LC, Cook MN, Brown KK, Duraiswami C, Bertin J, and Gough PJ (2012). Autolytic proteolysis within the function to find domain (FIIND) is required for NLRP1 inflammasome activity. *J. Biol. Chem.* 287, 25030–25037. 10.1074/jbc.M112.378323. [PubMed: 22665479]
6. Frew BC, Joag VR, and Mogridge J (2012). Proteolytic processing of Nlrp1b is required for inflammasome activity. *PLoS Pathog.* 8, e1002659. 10.1371/journal.ppat.1002659. [PubMed: 22536155]
7. Sandstrom A, Mitchell PS, Goers L, Mu EW, Lesser CF, and Vance RE (2019). Functional degradation: a mechanism of NLRP1 inflammasome activation by diverse pathogen enzymes. *Science* 364, eaau1330. 10.1126/science.aau1330. [PubMed: 30872533]
8. Chui AJ, Okondo MC, Rao SD, Gai K, Griswold AR, Johnson DC, Ball DP, Taabazuig CY, Orth EL, Vittimberga BA, and Bachovchin DA (2019). N-terminal degradation activates the NLRP1B inflammasome. *Science* 364, 82–85. 10.1126/science.aau1208. [PubMed: 30872531]
9. Zhong FL, Robinson K, Teo DET, Tan KY, Lim C, Harapas CR, Yu CH, Xie WH, Sobota RM, Au VB, et al. (2018). Human DPP9 represses NLRP1 inflammasome and protects against autoinflammatory diseases via both peptidase activity and FIIND domain binding. *J. Biol. Chem.* 293, 18864–18878. 10.1074/jbc.RA118.004350. [PubMed: 30291141]
10. Hollingsworth LR, Sharif H, Griswold AR, Fontana P, Mintseris J, Dagbay KB, Paulo JA, Gygi SP, Bachovchin DA, and Wu H (2021). DPP9 sequesters the C terminus of NLRP1 to repress inflammasome activation. *Nature* 592, 778–783. 10.1038/s41586-021-03350-4. [PubMed: 33731932]

11. Huang M, Zhang X, Toh GA, Gong Q, Wang J, Han Z, Wu B, Zhong F, and Chai J (2021). Structural and biochemical mechanisms of NLRP1 inhibition by DPP9. *Nature* 592, 773–777. 10.1038/s41586-021-03320-w. [PubMed: 33731929]
12. Sharif H, Hollingsworth LR, Griswold AR, Hsiao JC, Wang Q, Bachovchin DA, and Wu H (2021). Dipeptidyl peptidase 9 sets a threshold for CARD8 inflammasome formation by sequestering its active C-terminal fragment. *Immunity* 54, 1392–1404.e10. 10.1016/j.immuni.2021.04.024. [PubMed: 34019797]
13. Mitchell PS, Sandstrom A, and Vance RE (2019). The NLRP1 inflammasome: new mechanistic insights and unresolved mysteries. *Curr. Opin. Immunol.* 60, 37–45. 10.1016/j.coi.2019.04.015. [PubMed: 31121538]
14. Boyden ED, and Dietrich WF (2006). Nalp1b controls mouse macrophage susceptibility to anthrax lethal toxin. *Nat. Genet.* 38, 240–244. 10.1038/ng1724. [PubMed: 16429160]
15. Robinson KS, Teo DET, Tan KS, Toh GA, Ong HH, Lim CK, Lay K, Au BV, Lew TS, Chu JJH, et al. (2020). Enteroviral 3C protease activates the human NLRP1 inflammasome in airway epithelia. *Science* 370, eaay2002. 10.1126/science.aay2002. [PubMed: 33093214]
16. Tsu BV, Beierschmitt C, Ryan AP, Agarwal R, Mitchell PS, and Daugherty MD (2020). Diverse viral proteases activate the NLRP1 inflammasome. Preprint at bioRxiv. 10.1101/2020.10.16.343426.
17. Hornung V, Ablasser A, Charrel-Dennis M, Bauernfeind F, Horvath G, Caffrey DR, Latz E, and Fitzgerald KA (2009). AIM2 recognizes cytosolic dsDNA and forms a caspase-1-activating inflammasome with ASC. *Nature* 458, 514–518. 10.1038/nature07725. [PubMed: 19158675]
18. Wang Q, Gao H, Clark KM, Mugisha CS, Davis K, Tang JP, Harlan GH, DeSelm CJ, Presti RM, Kutluay SB, and Shan L (2021). CARD8 is an inflammasome sensor for HIV-1 protease activity. *Science* 371, eabe1707. 10.1126/science.abe1707. [PubMed: 33542150]
19. Gai K, Okondo MC, Rao SD, Chui AJ, Ball DP, Johnson DC, and Bachovchin DA (2019). DPP8/9 inhibitors are universal activators of functional NLRP1 alleles. *Cell Death Dis.* 10, 587. 10.1038/s41419-019-1817-5. [PubMed: 31383852]
20. Okondo MC, Johnson DC, Sridharan R, Go EB, Chui AJ, Wang MS, Poplawski SE, Wu W, Liu Y, Lai JH, et al. (2017). DPP8 and DPP9 inhibition induces pro-caspase-1-dependent monocyte and macrophage pyroptosis. *Nat. Chem. Biol.* 13, 46–53. 10.1038/nchembio.2229. [PubMed: 27820798]
21. Johnson DC, Taabazuing CY, Okondo MC, Chui AJ, Rao SD, Brown FC, Reed C, Peguero E, de Stanchina E, Kentsis A, and Bachovchin DA (2018). DPP8/DPP9 inhibitor-induced pyroptosis for treatment of acute myeloid leukemia. *Nat. Med.* 24, 1151–1156. 10.1038/s41591-018-0082-y. [PubMed: 29967349]
22. Tang HK, Tang HY, Hsu SC, Chu YR, Chien CH, Shu CH, and Chen X (2009). Biochemical properties and expression profile of human prolyl dipeptidase DPP9. *Arch. Biochem. Biophys.* 485, 120–127. 10.1016/j.abb.2009.02.015. [PubMed: 19268648]
23. Geiss-Friedlander R, Parmentier N, Möller U, Urlaub H, Van den Eynde BJ, and Melchior F (2009). The cytoplasmic peptidase DPP9 is rate-limiting for degradation of proline-containing peptides. *J. Biol. Chem.* 284, 27211–27219. 10.1074/jbc.M109.041871. [PubMed: 19667070]
24. Griswold AR, Cifani P, Rao SD, Axelrod AJ, Miele MM, Hendrickson RC, Kentsis A, and Bachovchin DA (2019). A chemical strategy for protease substrate profiling. *Cell Chem. Biol.* 26, 901–907.e6. 10.1016/j.chembiol.2019.03.007. [PubMed: 31006619]
25. Rao SD, Chen Q, Wang Q, Orth-He EL, Saoi M, Griswold AR, Bhattacharjee A, Ball DP, Huang HC, Chui AJ, et al. (2022). M24B aminopeptidase inhibitors selectively activate the CARD8 inflammasome. *Nat. Chem. Biol.* 18, 565–574. 10.1038/s41589-021-00964-7. [PubMed: 35165443]
26. Orth-He EL, Huang H-C, Rao SD, Wang Q, Chen Q, O’Mara CM, Chui AJ, Saoi M, Griswold A, Bhattacharjee A, et al. (2022). Protein Folding Stress Potentiates NLRP1 and CARD8 Inflammasome Activation. *Cell Reports.* 10.1016/j.celrep.2022.111965.
27. Ball DP, Tsamouri LP, Wang AE, Huang HC, Warren CD, Wang Q, Edmondson IH, Griswold AR, Rao SD, Johnson DC, and Bachovchin DA (2022). Oxidized thioredoxin-1 restrains the NLRP1 inflammasome. *Sci. Immunol* 7, eabm7200. 10.1126/sciimmunol.abm7200. [PubMed: 36332009]

28. Okondo MC, Rao SD, Taabazuing CY, Chui AJ, Poplawski SE, Johnson DC, and Bachovchin DA (2018). Inhibition of dpp8/9 activates the Nlrp1b inflammasome. *Cell Chem. Biol.* 25, 262–267.e5. 10.1016/j.chembiol.2017.12.013.
29. Dixon SJ, Lemberg KM, Lamprecht MR, Skouta R, Zaitsev EM, Gleason CE, Patel DN, Bauer AJ, Cantley AM, Yang WS, et al. (2012). Ferroptosis: an iron-dependent form of nonapoptotic cell death. *Cell* 149, 1060–1072. 10.1016/j.cell.2012.03.042. [PubMed: 22632970]
30. Conlon M, Poltorack CD, Forcina GC, Armenta DA, Mallais M, Perez MA, Wells A, Kahanu A, Magtanong L, Watts JL, et al. (2021). A compendium of kinetic modulatory profiles identifies ferroptosis regulators. *Nat. Chem. Biol.* 17, 665–674. 10.1038/s41589-021-00751-4. [PubMed: 33686292]
31. Johnson DC, Okondo MC, Orth EL, Rao SD, Huang HC, Ball DP, and Bachovchin DA (2020). DPP8/9 inhibitors activate the CARD8 inflammasome in resting lymphocytes. *Cell Death Dis.* 11, 628. 10.1038/s41419-020-02865-4. [PubMed: 32796818]
32. Linder A, Bauernfried S, Cheng Y, Albanese M, Jung C, Keppler OT, and Hornung V (2020). CARD8 inflammasome activation triggers pyroptosis in human T cells. *EMBO J.* 39, e105071. 10.15252/embj.2020105071. [PubMed: 32840892]
33. Ball DP, Taabazuing CY, Griswold AR, Orth EL, Rao SD, Kotliar IB, Vostal LE, Johnson DC, and Bachovchin DA (2020). Caspase-1 interdomain linker cleavage is required for pyroptosis. *Life Sci. Alliance* 3, e202000664. 10.26508/lsa.202000664. [PubMed: 32051255]
34. Chui AJ, Griswold AR, Taabazuing CY, Orth EL, Gai K, Rao SD, Ball DP, Hsiao JC, and Bachovchin DA (2020). Activation of the CARD8 inflammasome requires a disordered region. *Cell Rep.* 33, 108264. 10.1016/j.celrep.2020.108264. [PubMed: 33053349]
35. Nabet B, Roberts JM, Buckley DL, Paulk J, Dastjerdi S, Yang A, Leggett AL, Erb MA, Lawlor MA, Souza A, et al. (2018). The dTAG system for immediate and target-specific protein degradation. *Nat. Chem. Biol.* 14, 431–441. 10.1038/s41589-018-0021-8. [PubMed: 29581585]
36. Van Goethem S, Van der Veken P, Dubois V, Soroka A, Lambeir AM, Chen X, Haemers A, Scharpé S, De Meester I, and Augustyns K (2008). Inhibitors of dipeptidyl peptidase 8 and dipeptidyl peptidase 9. Part 2: isoindoline containing inhibitors. *Bioorg. Med. Chem. Lett.* 18, 4159–4162. 10.1016/j.bmcl.2008.05.079. [PubMed: 18556198]
37. Yang WS, SriRamaratnam R, Welsch ME, Shimada K, Skouta R, Viswanathan VS, Cheah JH, Clemons PA, Shamji AF, Clish CB, et al. (2014). Regulation of ferroptotic cancer cell death by GPX4. *Cell* 156, 317–331. 10.1016/j.cell.2013.12.010. [PubMed: 24439385]
38. Conlon M, Poltorack C, Forcina GC, Wells A, Mallais M, Kahanu A, Magtanong L, Pratt DA, and Dixon SJ (2019). A compendium of kinetic cell death modulatory profiles identifies ferroptosis regulators. Preprint at bioRxiv. 826925. 10.1101/826925.
39. Ingold KU, and Pratt DA (2014). Advances in radical-trapping antioxidant chemistry in the 21st century: a kinetics and mechanisms perspective. *Chem. Rev.* 114, 9022–9046. 10.1021/cr500226n. [PubMed: 25180889]
40. Shah R, Poon JF, Haidasz EA, and Pratt DA (2021). Temperature-dependent effects of alkyl substitution on diarylamine antioxidant reactivity. *J. Org. Chem.* 86, 6538–6550. 10.1021/acs.joc.1c00365. [PubMed: 33900079]
41. Cirelli KM, Gorfu G, Hassan MA, Printz M, Crown D, Leppla SH, Grigg ME, Saeij JPI, and Moayeri M (2014). Inflammasome sensor NLRP1 controls rat macrophage susceptibility to *Toxoplasma gondii*. *PLoS Pathog.* 10, e1003927. 10.1371/journal.ppat.1003927. [PubMed: 24626226]
42. Ewald SE, Chavarria-Smith J, and Boothroyd JC (2014). NLRP1 is an inflammasome sensor for *Toxoplasma gondii*. *Infect. Immun.* 82, 460–468. 10.1128/IAI.01170-13. [PubMed: 24218483]
43. Hsiao JC, Neugroschl AR, Chui AJ, Taabazuing CY, Griswold AR, Wang Q, Huang HC, Orth-He EL, Ball DP, Hiotis G, and Bachovchin DA (2022). A ubiquitin-independent proteasome pathway controls activation of the CARD8 inflammasome. *J. Biol. Chem.* 298, 102032. 10.1016/j.jbc.2022.102032. [PubMed: 35580636]
44. Tu BP, and Weissman JS (2004). Oxidative protein folding in eukaryotes: mechanisms and consequences. *J. Cell Biol.* 164, 341–346. 10.1083/jcb.200311055. [PubMed: 14757749]

45. Ray PD, Huang BW, and Tsuji Y (2012). Reactive oxygen species (ROS) homeostasis and redox regulation in cellular signaling. *Cell. Signal.* 24, 981–990. 10.1016/j.cellsig.2012.01.008. [PubMed: 22286106]
46. Manford AG, Rodriguez-Perez F, Shih KY, Shi Z, Berdan CA, Choe M, Titov DV, Nomura DK, and Rape M (2020). A cellular mechanism to detect and alleviate reductive stress. *Cell.* 10.1016/j.cell.2020.08.034.
47. Dickson MA, Hahn WC, Ino Y, Ronfard V, Wu JY, Weinberg RA, Louis DN, Li FP, and Rheinwald JG (2000). Human keratinocytes that express hTERT and also bypass a p16^{INK4a}-enforced mechanism that limits life span become immortal yet retain normal growth and differentiation characteristics. *Mol. Cell Biol.* 20, 1436–1447. 10.1128/MCB.20.4.1436-1447.2000. [PubMed: 10648628]
48. Doench JG, Fusi N, Sullender M, Hegde M, Vaimberg EW, Donovan KF, Smith I, Tothova Z, Wilen C, Orchard R, et al. (2016). Optimized sgRNA design to maximize activity and minimize off-target effects of CRISPR-Cas9. *Nat. Biotechnol.* 34, 184–191. 10.1038/nbt.3437. [PubMed: 26780180]
49. Amzallag A, Ramaswamy S, and Benes CH (2019). Statistical assessment and visualization of synergies for large-scale sparse drug combination datasets. *BMC Bioinf.* 20, 83. 10.1186/s12859-019-2642-7.
50. Liu Q, Yin X, Languino LR, and Altieri DC (2018). Evaluation of drug combination effect using a Bliss independence dose-response surface model. *Stat. Biopharm. Res.* 10, 112–122. 10.1080/19466315.2018.1437071. [PubMed: 30881603]

Highlights

- Radical-trapping antioxidants, including JSH-23, induce reductive stress
- JSH-23 accelerates the degradation of the NLRP1- and CARD8-repressive N-terminal fragments
- JSH-23 synergizes with DPP8/9 inhibitors to induce NLRP1 and CARD8 inflammasome activation

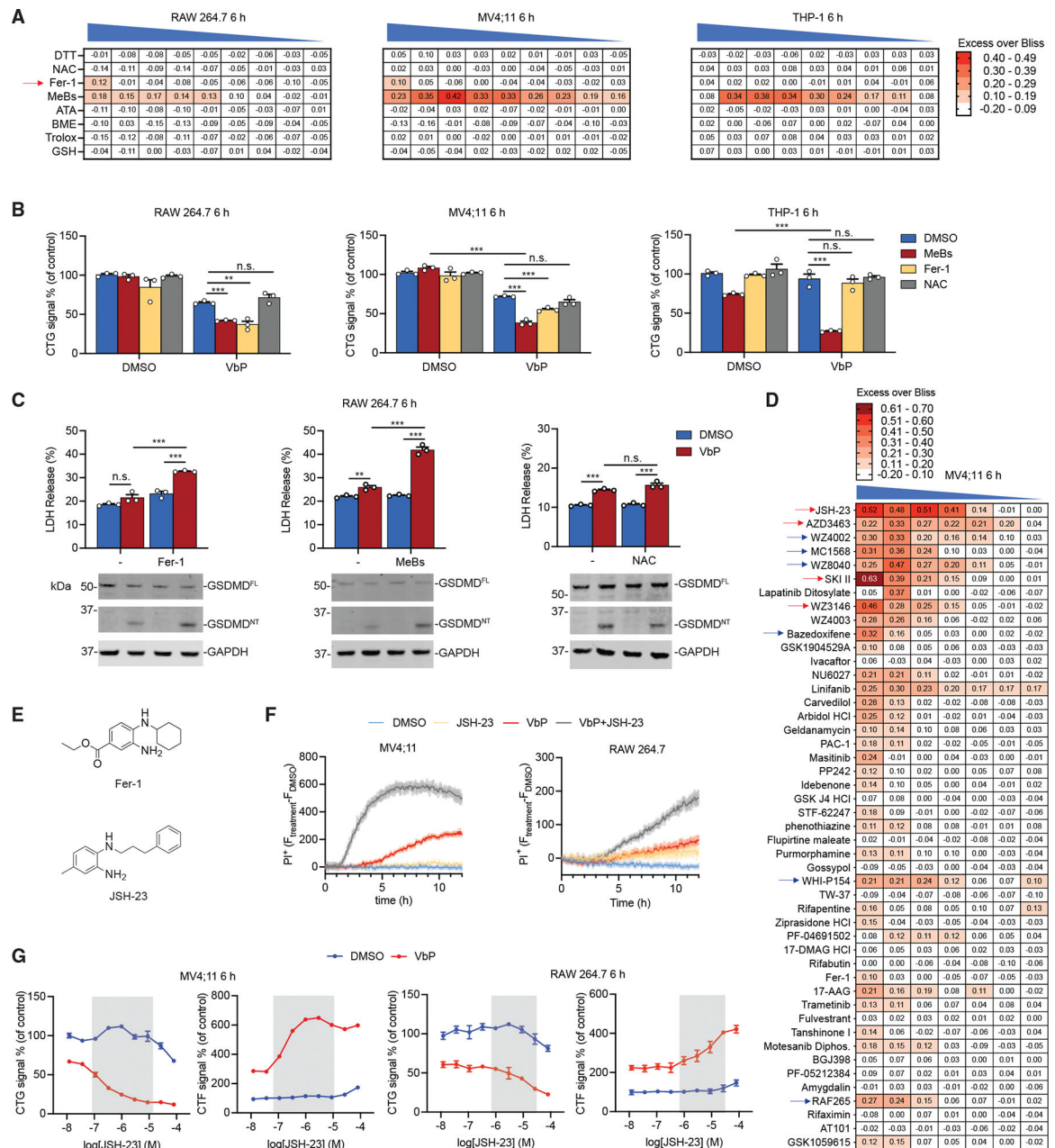


Figure 1. Ferroptosis inhibitors synergize with VbP

(A) The indicated cells were treated with the varying doses of the indicated compounds \pm VbP (10 μ M) for 6 h before cell viability was evaluated by CTG. For each pair of concentrations, we subtracted the predicted Bliss additive effect from the observed inhibition. Values greater than zero indicate synergy. Compounds were all tested in 3-fold dilution series from the following highest doses: DTT (2 mM); NAC (4 mM); Fer-1 (40 μ M); MeBs (20 μ M); α -tocopherol acetate (ATA) (2 mM); β -mercaptoethanol (BME) (4 mM); trolox (400 μ M); and GSH (1 mM) (n = 3).

(B) The indicated cells were treated with MeBs (6.7 μ M), Fer-1 (40 μ M), and NAC (4 mM) \pm VbP (10 μ M) for 6 h before CTG analysis (n = 3).

(C) RAW 264.7 cells were treated with Fer-1 (40 μ M), MeBs (20 μ M), and NAC (2 mM) \pm VbP (10 μ M) for 6 h before cell death was assessed by LDH release and immunoblot analyses (n = 3).

(D) MV4;11 cells were treated with varying doses of ferroptosis inhibitors \pm VbP (10 μ M) for 6 h before cell viability was measured by CTG. For each pair of concentrations, we subtracted the predicted Bliss additive effect from the observed inhibition. All compounds were tested in 3-fold dilution series. The highest dose of phenothiazine was 400 μ M; the highest doses of MC1568, amygdalin, gossypol, idebenone, SKI II, flupirtine maleate, carvedilol, rifaximin, masitinib, ferrostatin-1, WHI-P154, AT101, STF-62247, WZ4002, JSH-23, 17-AAG, NU6027, motesanib diphosphate, arbidol HCl, PAC-1, GSK J4 HCl, and PP242 were 80 μ M; the highest doses of all others were 40 μ M. Red and blue arrows indicate compounds further investigated in this article (n = 3).

(E) Structures of ferrostatin-1 (Fer-1) and JSH-23.

(F) MV4;11 and RAW 264.7 cells were treated with JSH-23 (10 μ M in MV4;11 cells and 1 μ M in RAW 264.7 cells), VbP (10 μ M), or both before cell death was assessed by PI uptake (n = 6).

(G) MV4;11 and RAW 264.7 cells were treated with the indicated concentrations of JSH-23 and VbP (10 μ M) for 6 h before CTG or CTF analyses (n = 3). Synergistic cell death is highlighted in gray.

Data are means \pm SEM. ***p < 0.001, **p < 0.01, by two-sided Student's t test. n.s., not significant. All data, including immunoblots, are representative of three or more independent experiments.

See also Figure S2.

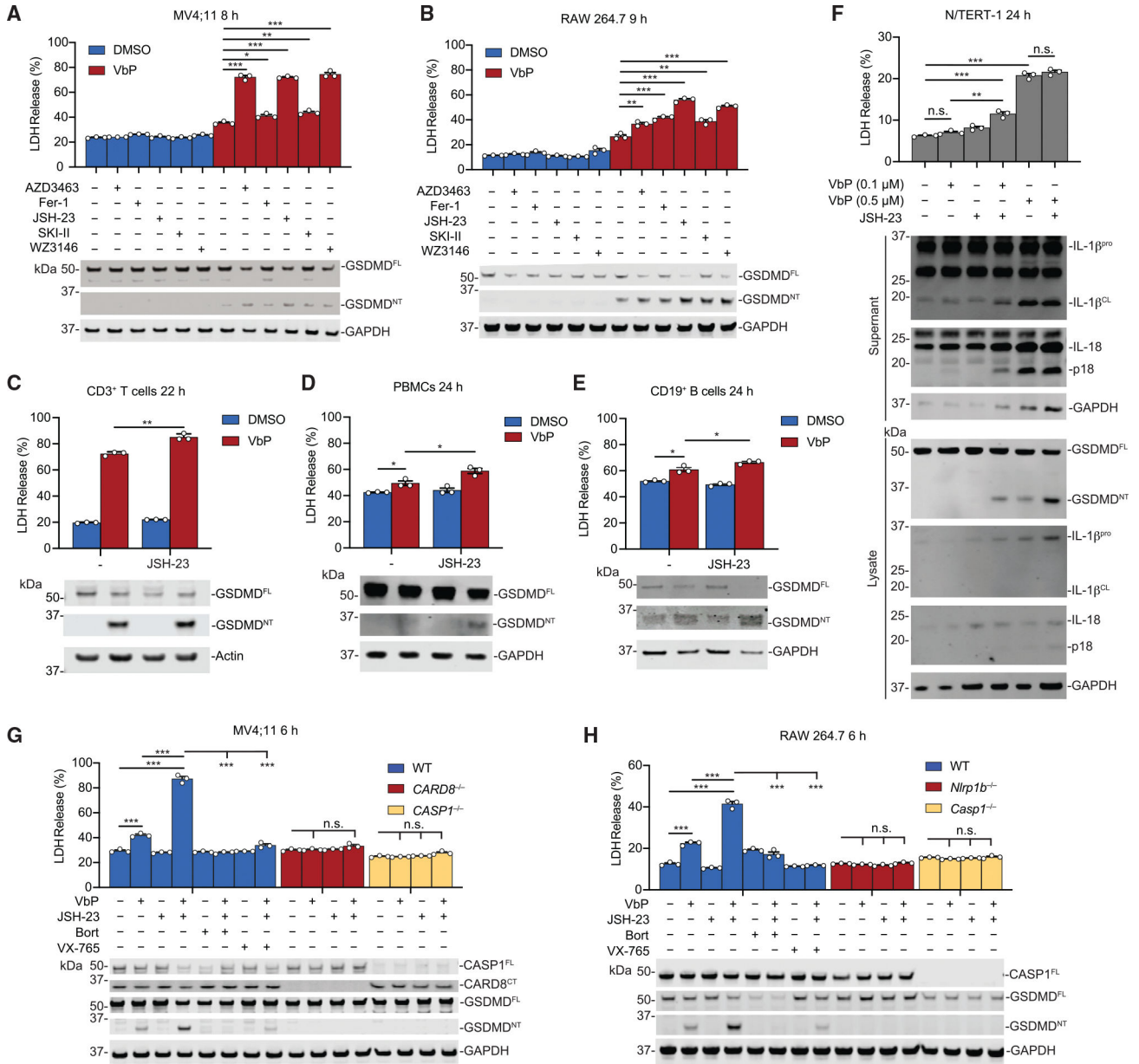


Figure 2. Ferroptosis inhibitors increase CARD8 and NLRP1 inflammasome activation
 (A and B) MV4;11 and RAW 264.7 cells were treated with AZD3463 (1 μM); Fer-1 (20 μM); JSH-23 (1 μM); SKI II (20 μM for MV4;11 cells and 10 μM for RAW 264.7 cells); and WZ3146 (4 μM) ± VbP (10 μM) for the indicated times before LDH release and immunoblot analyses (n = 3).
 (C–E) Resting human CD3⁺ T cells (C), human primary peripheral blood mononuclear cells (PBMCs; D), and human peripheral blood CD19⁺ B cells (E) were treated with JSH-23 (10 μM for C and 5 μM for D and E), VbP (0.2 μM for C and 10 μM for D and E), or both for the indicated times before LDH release and immunoblot analyses (n = 3).
 (F) N/TERT-1 keratinocytes were treated with JSH-23 (2 μM) ± VbP for 24 h before LDH release and immunoblot analyses (n = 3).

(G and H) MV4;11 and RAW 264.7 cells were treated with bortezomib (Bort; 1 μ M) or VX-765 (10 μ M) for 15 min followed by treatment with VbP (10 μ M), JSH-23 (1 μ M), or both before LDH release and immunoblot analyses (n = 3).

Data are means \pm SEM. ***p < 0.001, **p < 0.01, *p < 0.05 by two-sided Student's t test. n.s., not significant. All data, including immunoblots, are representative of three or more independent experiments.

See also Figure S3.

Author Manuscript

Author Manuscript

Author Manuscript

Author Manuscript

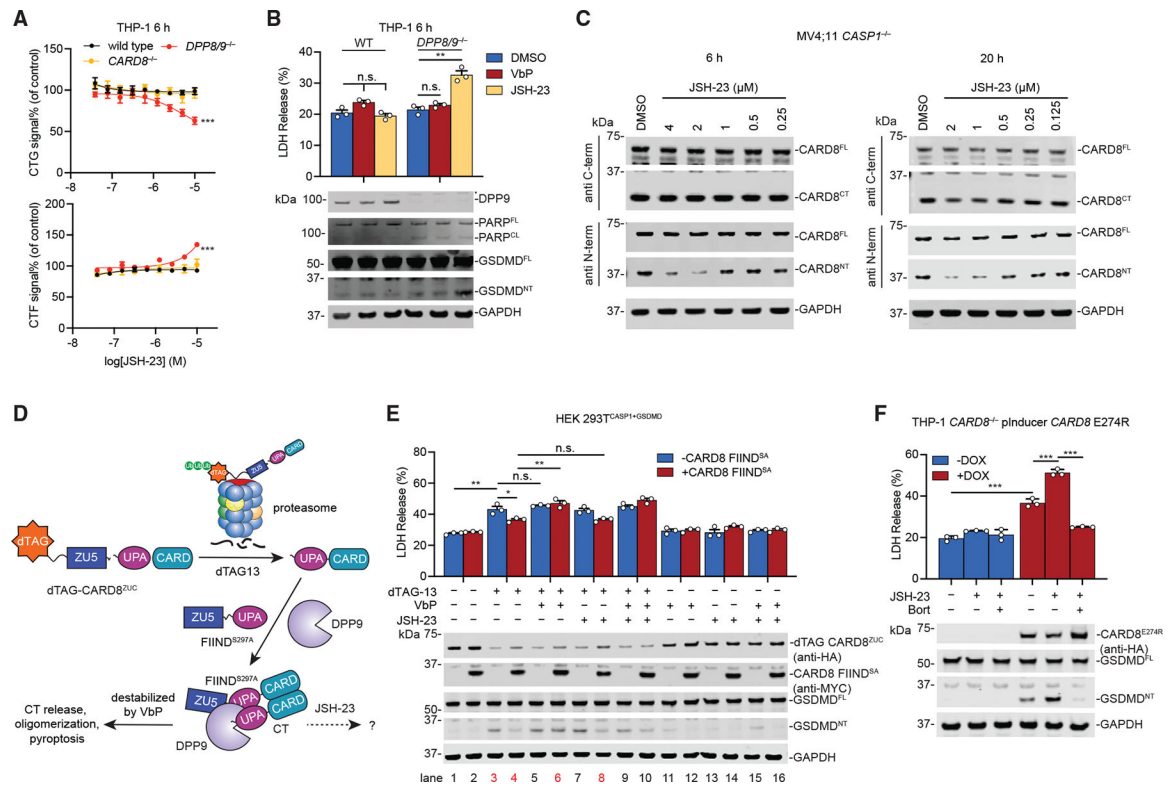


Figure 3. JSH-23 accelerates NT degradation

(A and B) WT, *DPP8/9*^{-/-}, or *CARD8*^{-/-} THP-1 cells were treated with VbP (10 μM) or JSH-23 (2 μM in B) for 6 h prior to CTG (A) (n = 4) and LDH release and immunoblot analyses (B) (n = 3).

(C) *CASP1*^{-/-} MV4;11 cells were treated with the indicated concentrations of JSH-23 for 6 (left) or 20 h (right). CARD8 protein levels were then evaluated by immunoblotting.

(D) Schematic of dTAG-based assay used to evaluate the ability of compounds to destabilize the CARD8-DPP8/9 ternary complex in cells.

(E) HEK293T cells stably expressing CASP1 and GSDMD were transiently transfected with plasmids encoding dTAG-CARD8^{ZUC} and CARD8 FIIND^{S297A}. Cells were treated with dTAG-13 (500 nM), VbP (10 μM), and JSH-23 (2 μM) for 3 h before LDH release and immunoblot analyses (n = 3).

(F) *CARD8*^{-/-} THP-1 cells containing a dox-inducible CARD8 E274R mutant that does not bind to DPP8/9 were pre-treated with or without DOX (100 ng/mL, 16 h), and then treated with JSH-23 (5 μM) ± Bort (1 μM) for 6 h, followed by LDH release and immunoblot analyses (n = 3).

Data are means ± SEM. ***p < 0.001, **p < 0.01, *p < 0.05 by two-sided Student's t test.

n.s., not significant. All data, including immunoblots, are representative of three or more independent experiments.

See also Figure S4.

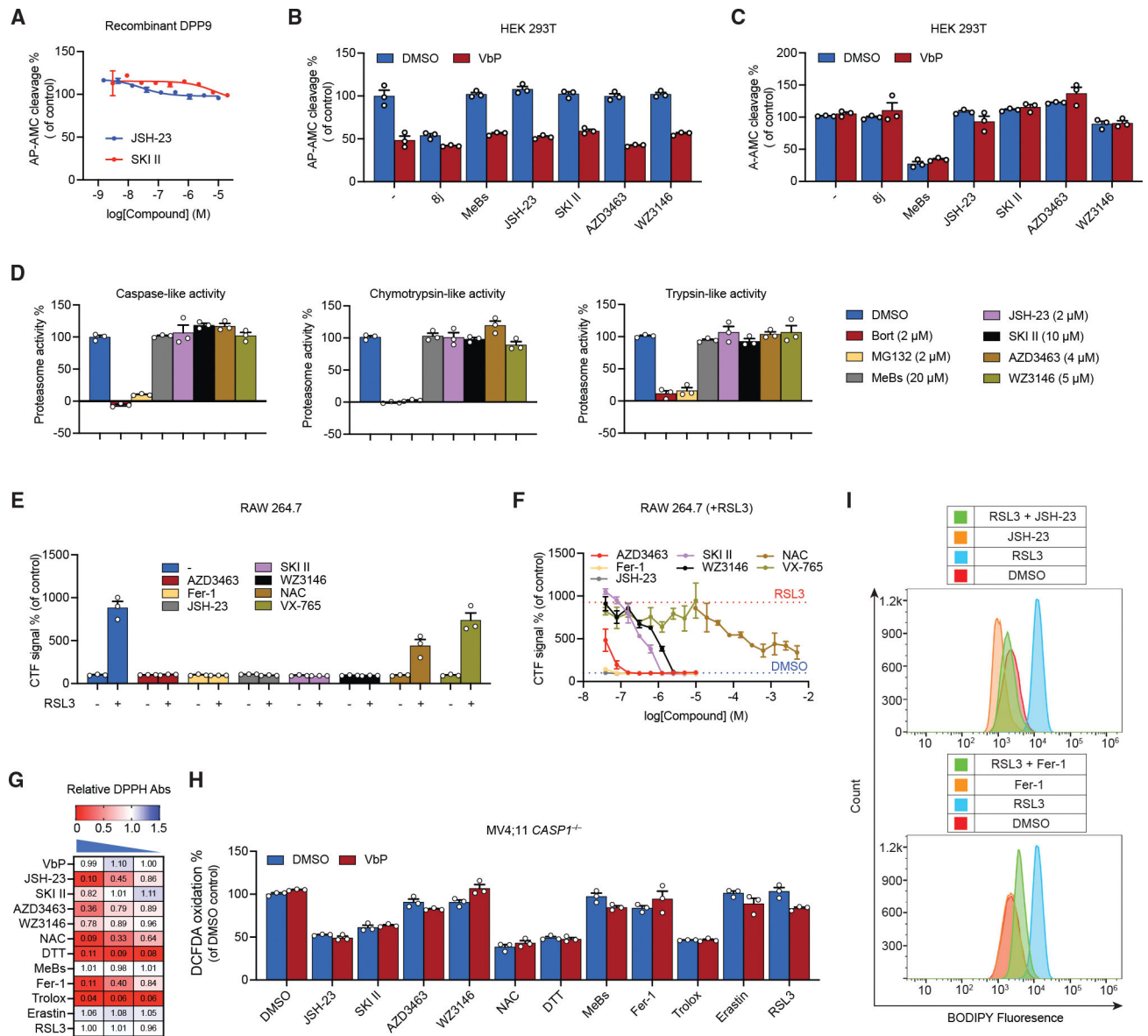


Figure 4. Synergistic compounds are radical-trapping agents that induce reductive stress

(A) The indicated concentrations of JSH-23 and SKI-II do not inhibit the activity of recombinant DPP9 in an AP-AMC assay ($n = 3$).

(B and C) HEK293T cells were treated with 8j (10 μ M); MeBs (20 μ M); JSH-23 (5 μ M); SKI II (10 μ M); AZD3463 (1 μ M); or WZ3146 (4 μ M) \pm VbP (10 μ M) before assaying for AP-AMC (B) or A-AMC (C) cleavage ($n = 3$).

(D) The ferroptosis inhibitors do not impact proteasome activity in the cell-based proteasome-Glo assay ($n = 3$).

(E and F) RAW 264.7 cells were treated with the indicated compounds \pm RSL3 (0.25 μ M). Cell death was evaluated by CTF after 4.5 h ($n = 3$). All compounds in (E) were tested at 5 μ M (except for NAC at 1.2 mM).

(G) VbP (10 μ M); JSH-23 (10 μ M); SKI II (10 μ M); AZD3463 (10 μ M); WZ3146 (10 μ M); NAC (0.5 mM); DTT (0.5 mM); MeBs (10 μ M); Fer-1 (25 μ M); trolox (200 μ M); erastin (10

μM); and RSL3 (0.25 μM) were tested for radical-trapping activity using a cell-free DPPH assay ($n = 3$). The highest concentration for each compound is indicated above, which was then diluted 5-fold serially.

(H) VbP (10 μM); JSH-23 (4 μM); SKI II (20 μM); AZD3463 (4 μM); WZ3146 (0.8 μM); NAC (1 mM); DTT (1 mM); MeBs (20 μM); Fer-1 (0.8 μM); trolox (400 μM); erastin (20 μM); and RSL3 (0.5 μM) \pm VbP (10 μM) were tested for their impact on the oxidation of the cell-permeable H₂DCFDA probe in *CASP1*^{-/-} MV4;11 cells ($n = 3$).

(I) *Casp1*^{-/-} RAW 264.7 cells were treated with JSH-23 (1 μM), Fer-1 (1 μM), RSL3 (1 μM), or the indicated combinations for 2 h prior to assessing the oxidation of the C11 BODIPY 581/591 probe.

Data are means \pm SEM. All data are representative of three or more independent experiments.

See also Figure S5.

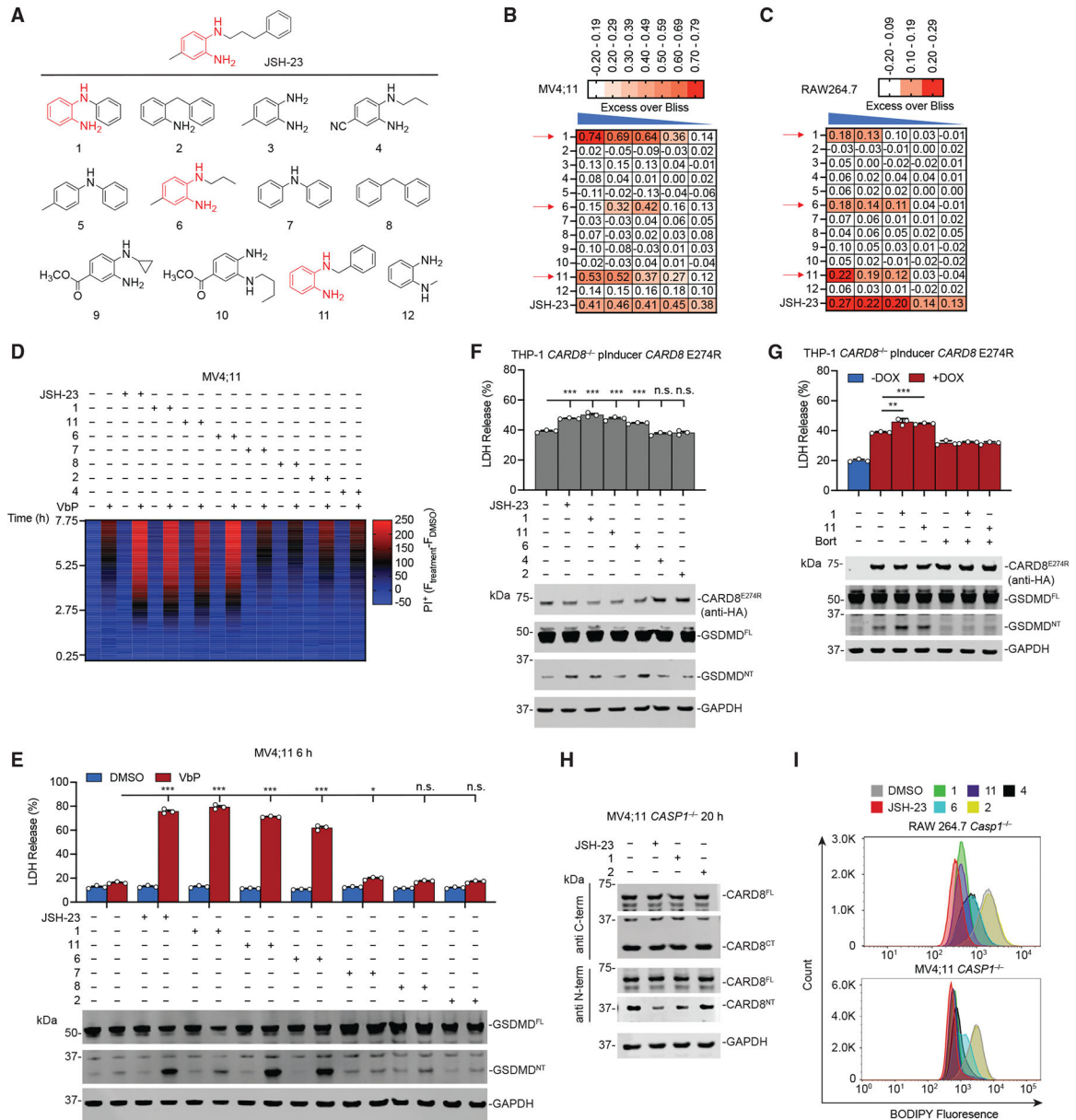


Figure 5. Structure-activity relationship of JSH-23

(A) Structures of JSH-23 derivatives.

(B and C) MV4;11 (B) and RAW 264.7 (C) cells were treated with the varying doses of the indicated compounds (the highest concentration for each is 40 μ M, followed by serial 3-fold dilutions) \pm VbP (10 μ M) for 6 h before cell viability was evaluated by CTG (n = 3). For each pair of concentrations, we subtracted the predicted Bliss additive effect from the observed inhibition.

(D and E) MV4;11 cells were treated with the indicated JSH-23 derivative (5 μ M) \pm VbP (10 μ M) prior to assessing cell death by PI uptake over 8 h (D) (n = 3) or by LDH release and immunoblot analyses after 6 h (E) (n = 3).

(F and G) *CARD8*^{-/-} THP-1 cells containing a DPP9 non-binding *CARD8* E274R mutant were treated with DOX (100 ng/mL, 16 h, F) or with or without DOX (100 ng/mL, 16 h, G)

followed by Bort (1 μM), JSH-23 (2 μM), compounds 1, 2, 4, 6, or 11 (all were tested at 5 μM), or the indicated combinations for 6 h prior to LDH release and immunoblot analyses ($n = 3$).

(H) *CASP1*^{-/-} MV4;11 cells were treated with JSH-23 or compounds 1 or 2 (all 2 μM) for 20 h before immunoblot analysis.

(I) Compounds 1, 2, 4, 6, and 11 (all at 5 μM for 2 h) were tested for their impact on lipid ROS in *Casp1*^{-/-} RAW 264.7 using the C11 BODIPY 581/591 probe.

Data are means \pm SEM. *** $p < 0.001$, ** $p < 0.01$, * $p < 0.05$ by two-sided Student's t test. n.s., not significant. All data, including immunoblots, are representative of three or more independent experiments.

See also Figure S6.

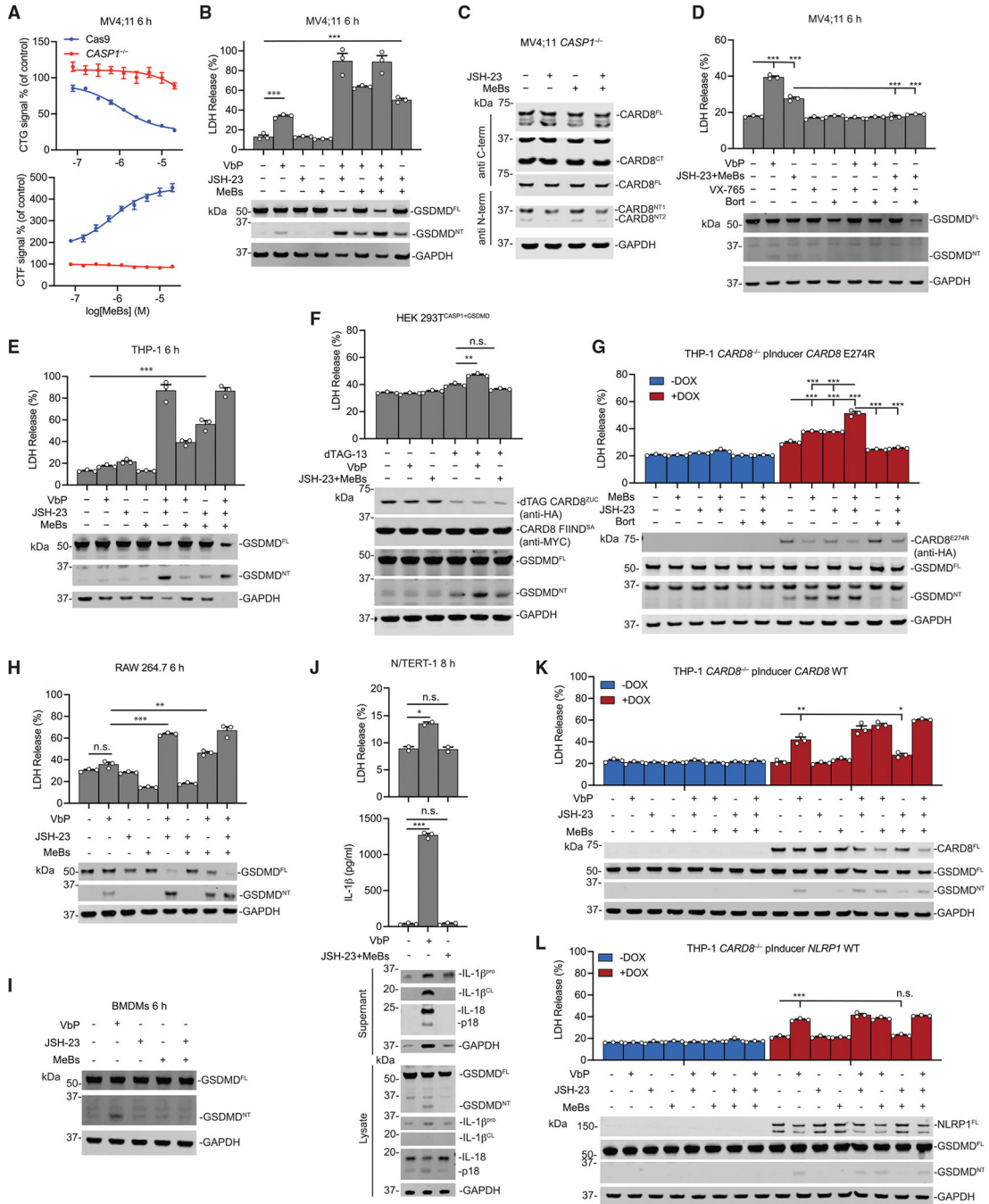


Figure 6. AP inhibitors and RTAs activate CARD8 inflammasome

(A) Control (Cas9) or *CASP1*^{-/-} MV4;11 cells were treated with JSH-23 (5 μ M) and the indicated concentration of MeBs for 6 h before cell viability was evaluated by CTG and CTF (n = 3).

(B–E) The indicated cells were treated with JSH-23 (2 μ M), MeBs (10 μ M), VX-765 (50 μ M), Bort (1 μ M), or the specified combinations for 6 h prior to LDH release and immunoblot analyses (n = 3). VX-765 and Bort were applied 30 min before the inflammasome inducers.

(F) HEK293T cells stably expressing CASP1 and GSDMD were transiently transfected with plasmids encoding dTAG-CARD8^{ZUC} and CARD8 FIIND^{S297A}. Cells were treated with dTAG-13 (500 nM), VbP (10 μ M), JSH-23 (2 μ M), and MeBs (10 μ M) for 3 h before LDH release and immunoblot analyses (n = 3).

(G) *CARD8*^{-/-} THP-1 cells containing a DOX-inducible DPP9 non-binding CARD8 E274R protein were treated with or without DOX (100 ng/mL, 16 h) before the addition of JSH-23 (5 μ M), MeBs (10 μ M), and Bort (1 μ M) for 6 h prior to LDH release and immunoblot analyses (n = 3). Bort was applied 30 min before the inflammasome inducers.

(H–J) The indicated cells were treated with JSH-23 (2 μ M), MeBs (10 μ M), VbP (10 μ M), or the specified combinations for the indicated time intervals before LDH release, IL-1 β release, and immunoblotting analysis (n = 3 for H and IL-1 β release assay in J and n = 2 for LDH assay in J).

(K and L) *CARD8*^{-/-} THP-1 cells containing either a DOX-inducible CARD8 protein or NLRP1 protein were treated with or without DOX (100 ng/mL for CARD8 and 1 μ g/mL for NLRP1, 16 h) before the addition of JSH-23 (2 μ M), MeBs (10 μ M), or the specified combinations for 6 h prior to LDH release and immunoblot analyses (n = 3).

Data are means \pm SEM. ***p < 0.001, **p < 0.01, *p < 0.05 by two-sided Student's t test. n.s., not significant. All data, including immunoblots, are representative of three or more independent experiments.

See also Figure S7.

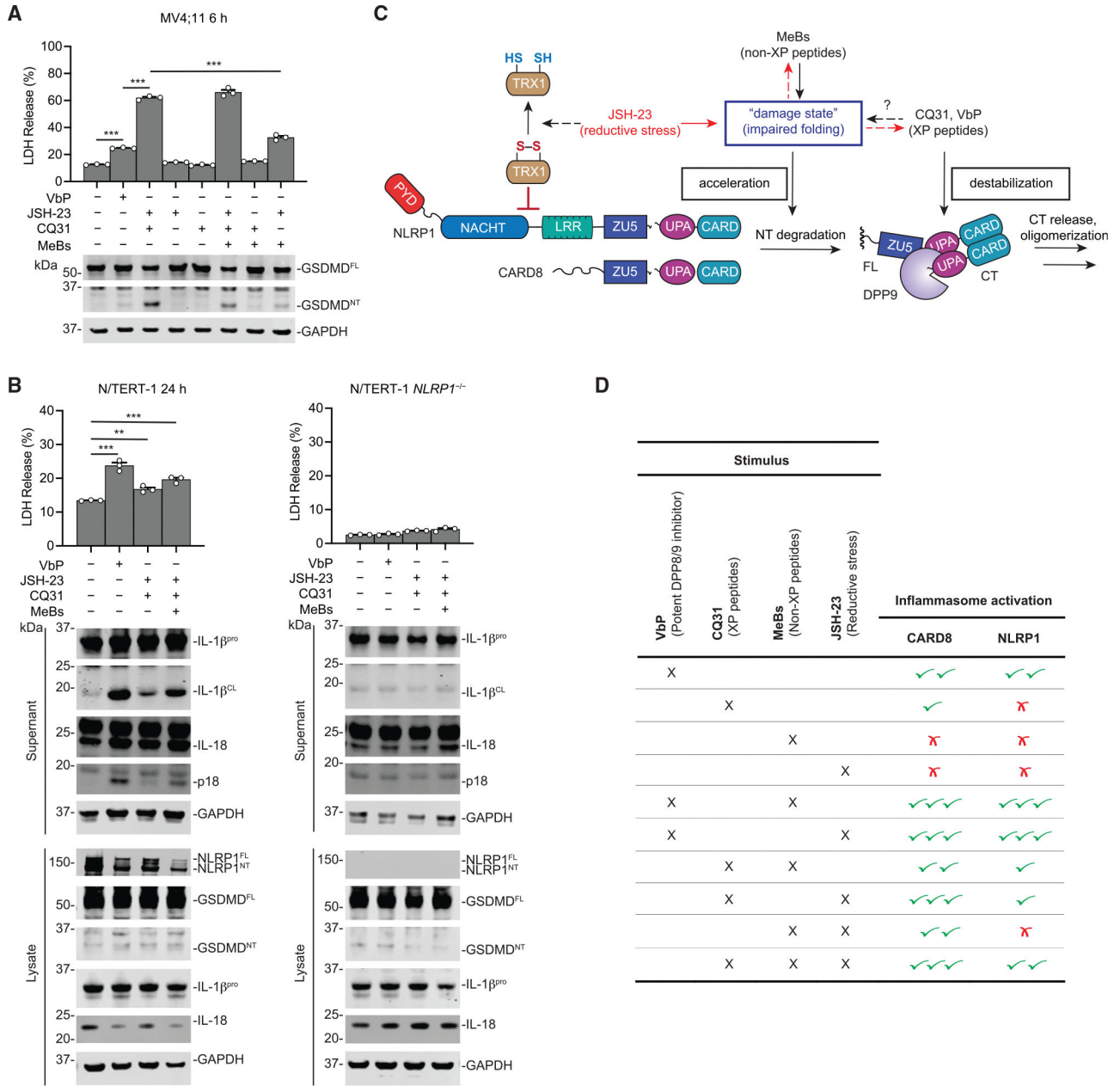


Figure 7. XP peptide accumulation and reductive stress activates NLRP1
 (A and B) The indicated cells were treated with JSH-23 (2 μM), MeBs (10 μM), CQ31 (10 μM in A and 5 μM in B), or the specified combinations for the indicated time intervals (n = 3). Data are means ± SEM. ***p < 0.001, **p < 0.01 by two-sided Student’s t test. n.s., not significant. All data, including immunoblots, are representative of three or more independent experiments.
 (C) The proposed danger signals that CARD8 and NLRP1 detect.
 (D) Summary of small-molecule NLRP1 and CARD8 activators.
 See also Figure S7.

KEY RESOURCES TABLE

REAGENT or RESOURCE	SOURCE	IDENTIFIER
Antibodies		
GSDMD Rabbit polyclonal Ab	Novus Biologicals	NBP2-33422; RRID: AB_2687913
CARD8 C-terminal rabbit polyclonal Ab	Abcam	ab24186; RRID: AB_2275096
CARD8 N-terminal rabbit polyclonal Ab	Abcam	ab194585
NLRP1 sheep polyclonal Ab	R&D Systems	AF-6788; RRID: AB_10891878
CASP1 rabbit polyclonal Ab	Cell Signaling Tech	2225S; RRID: AB_2243894
Mouse Casp1 rabbit polyclonal Ab	AdipoGen	AG-20B-0042; RRID: AB_2490248
PARP rabbit polyclonal Ab	Cell Signaling Tech	9542; RRID: AB_2160739
GAPDH (14C10) rabbit monoclonal Ab	Cell Signaling Tech	2118; RRID: AB_561053
Actin rabbit monoclonal Ab	Abcam	ab179467; RRID: AB_2737344
mouse GSDMD rabbit monoclonal Ab	Abcam	ab209845; RRID: AB_2783550
DPP9 rabbit monoclonal Ab	Abcam	ab42080; RRID: AB_731947
IL-1 β sheep polyclonal Ab	R&D Systems	AF-201; RRID: AB_354387
IL-18 sheep polyclonal Ab	R&D Systems	AF2548; RRID: AB_562603
ASC rabbit monoclonal Ab	AdipoGen	AG-25B-0006; RRID: AB_2490440
HA-Tag rabbit monoclonal Ab	Cell Signaling Tech	3724; RRID: AB_1549585
FLAG M2 monoclonal Ab	Millipore Sigma	F1804; RRID: AB_262044
IRDye 800CW anti-rabbit	LICOR	926-32213; RRID: AB_621848
IRDye 800CW anti-goat	LICOR	925-32214; RRID: AB_621846
IRDye 800CW anti-mouse	LICOR	926-32212; RRID: AB_621847
IRDye 680CW anti-mouse	LICOR	926-68072; RRID: AB_10953628
IRDye 680CW anti-rabbit	LICOR	925-68073; RRID: AB_2716687
Chemicals, peptides, and recombinant proteins		
Val-boroPro (VbP)	Cayman Chemical	29007
compound 8j (8j)	Okondo et al., 2017 ²⁰	N/A
Bortezomib (Bort.)	Millipore Sigma	504314
Bestatin methyl ester (MeBs)	Millipore Sigma	200485
CQ31	Rao et al., 2022 ²⁵	N/A
dTAG-13	R&D Systems	6605/5
MG132	Calbiochem	474787
VX765	Cayman Chemical	28825
Erastin	Cayman Chemical	17754
Sitagliptin	Thermo Fisher Scientific	11-101-5083
lipopolysaccharide (LPS)	Invivogen	tlrl-3pelps
Nigericin	Cayman Chemical	11437
Ala-Pro-7-amino-4-methylcoumarin (AP-AMC)	MP Biomedicals	03AMC04210
Ala-7-amino-4-methylcoumarin (A-AMC)	Millipore-Sigma	A4302
Doxycycline (DOX)	Cayman Chemical	14422
FuGENE HD	Promega	E2311

REAGENT or RESOURCE	SOURCE	IDENTIFIER
DL-Dithiothreitol	Millipore-Sigma	D9779
N-acetyl-L-cysteine	Cayman Chemical	20261
Ferrostatin-1	Cayman Chemical	17729
(±)- α -Tocopherol Acetate	Cayman Chemical	28399
β -Mercaptoethanol	Thermo Fisher Scientific	O34461
Trolox	Cayman Chemical	10011659
L-(-)-Glutathione (reduced form)	Thermo Fisher Scientific	AAA1801406
2,2-diphenyl-1-picrylhydrazyl	Thermo Fisher Scientific	D43131G
Propidium Iodide Solution	Cayman Chemical	10008351
JSH-23	ApexBio	B1645
AZD3463	Cayman Chemical	26172
WZ4002	ApexBio	A1389
MC1568	ApexBio	A4094
WZ8040	ApexBio	A1393
Sphingosine Kinase Inhibitor 2 (SKI II)	Cayman Chemical	10009222
Lapatinib Ditosylate	ApexBio	A3967
WZ3146	Cayman Chemical	23440
WZ4003	ApexBio	B1374
Bazedoxifene (acetate)	Cayman Chemical	15005
GSK1904529A	ApexBio	A1302
Ivacaftor	ApexBio	A5047
NU6027	ApexBio	A1986
Linifanib	ApexBio	A2949
Carvedilol	Cayman Chemical	15418
Arbidol HCl	ApexBio	A8362
Geldanamycin	ApexBio	A4060
PAC-1	ApexBio	A8177
Masitinib	Cayman Chemical	13105
PP242	ApexBio	A8318
Idebenone	Cayman Chemical	15475
GSK J4 HCl	ApexBio	A4190
STF-62247	ApexBio	B2151
phenothiazine	Thermo Fisher Scientific	P0106
Flupirtine maleate	Cayman Chemical	16674
Purmorphamine	Cayman Chemical	10009634
Gossypol	Cayman Chemical	14482
WHI-P154	ApexBio	A4150
TW-37	ApexBio	A4234
Rifapentine	ApexBio	B2127
Ziprasidone HCl	Cayman Chemical	15031
PF-04691502	ApexBio	A8499
17-DMAG HCl	ApexBio	A2213

REAGENT or RESOURCE	SOURCE	IDENTIFIER
Rifabutin	ApexBio	A2126
17-AAG	ApexBio	A4054
Trametinib	Cayman Chemical	16292
Fulvestrant	Cayman Chemical	10011269
Tanshinone I	Cayman Chemical	26852
Motesanib Diphos.	ApexBio	A5017
BGJ398	Cayman Chemical	19157
PF-05212384	ApexBio	B2179
Amygdalin	Cayman Chemical	26668
RAF265	ApexBio	A8313
Rifaximin	Cayman Chemical	16131
AT101	ApexBio	A3196
GSK1059615	Cayman Chemical	11569
RSL3	Cayman Chemical	19288
2-Aminodiphenylamine (derivative 1)	Thermo Fisher Scientific	A21295G
2-Aminodiphenylmethane (derivative 2)	Thermo Fisher Scientific	A25195G
3,4-Diaminotoluene (derivative 3)	Thermo Fisher Scientific	AC112431000
3-Amino-4-(propylamino)benzotrile (derivative 4)	Millipore-Sigma	COM448612726
4-Methyldiphenylamine (derivative 5)	Thermo Fisher Scientific	M11731G
4-methyl-N-1-propylbenzene-1,2-diamine (derivative 6)	Millipore-Sigma	ENA321762178
Diphenylamine (derivative 7)	Thermo Fisher Scientific	AC150740050
Diphenylmethane (derivative 8)	Thermo Fisher Scientific	D089625G
Methyl 3-amino-4-(cyclopropylamino)benzoate (derivative 9)	Millipore-Sigma	COM448617544
Methyl 4-amino-3-(butylamino)benzoate (derivative 10)	Millipore-Sigma	AMBH2D6FBDDD
N-Benzyl-1,2-diaminobenzene (derivative 11)	Santa Cruz Biotechnology	sc-358413
N-Methyl-1,2-phenylenediamine (derivative 12)	Thermo Fisher Scientific	AC434230050
Recombinant Human DPP9 Protein	R&D Systems	5419-SE
Critical commercial assays		
Pierce LDH Cytotoxicity Assay Kit	Life Technologies	PI88953
DC Protein Assay kit	Bio-Rad	5000111
IL-1 β ELISA Assay	R&D systems	SLB50
CellTiter-Glo Cell Viability Assay	Promega	G7573
CytoTox-Fluor cytotoxicity Assay	Promega	G9262
MycAlert Mycoplasma Detection Kit	Lonza	LT07-318
DCFDA / H2DCFDA Cellular ROS Assay Kit	Abcam	ab113851
Cell-Based Proteasome-Glo Assays	Promega	G1180
BODIPY 581/591 C11	Thermo Fisher Scientific	D3861
Deposited data		

REAGENT or RESOURCE	SOURCE	IDENTIFIER
Raw data underlying main and supplemental figures	This paper	https://doi.org/10.17632/8pvx4cw63h.1
Experimental models: Cell lines		
HEK293T	ATCC	CRL-3216
HEK293T <i>CASP1/GSDMD</i>	Johnson et al., 2018 ²¹	N/A
HEK293T <i>DPP9</i> ^{-/-}	This Study	N/A
THP-1	ATCC	TIB-202
THP-1 <i>CARD8</i> ^{-/-}	Johnson et al., 2018 ²¹	N/A
THP-1 <i>DPP8</i> ^{-/-} / <i>DPP9</i> ^{-/-}	Okondo et al., 2017 ²⁰	N/A
THP-1 <i>CARD8</i> ^{-/-} + pInducer20-CARD8-WT	Sharif et al., 2021 ¹²	N/A
THP-1 <i>CARD8</i> ^{-/-} + pInducer20-CARD8-E274R	Sharif et al., 2021 ¹²	N/A
THP-1 <i>CARD8</i> ^{-/-} + pInducer20-NLRP1-WT	This Study	N/A
THP-1 <i>CARD8</i> ^{-/-} + pInducer20-NLRP1-P1214R	This Study	N/A
RAW 264.7	ATCC	TIB-71
RAW 264.7 <i>Casp1</i> ^{-/-}	Okondo et al., 2017 ²⁰	N/A
RAW 264.7 <i>Nlrp1b</i> ^{-/-}	Chui et al., 2019 ⁸	N/A
RAW 264.7 ASC	This Study	N/A
MV4;11	DSMZ	N/A
MV4;11 <i>CARD8</i> ^{-/-}	Johnson et al., 2018 ²¹	N/A
MV4;11 <i>CASP1</i> ^{-/-}	Johnson et al., 2018 ²¹	N/A
N/TERT-1	Dickson et al., 2000 ⁴⁷	N/A
N/TERT-1 NLRP1 ^{-/-}	Ball et al., 2021 ²⁷	N/A
Naïve human CD3 T cells	HemaCare	Lot#21068415
Primary Peripheral Blood Mononuclear Cells (PBMCs)	ATCC	PCS-800-011
Human Peripheral Blood CD19+ B Cells	Stemcell Technologies	70033
OCI-AML2	DSMZ	ACC 99
Experimental models: Organisms/strains		
C57BL/6 mice (harvested BMDMs)	The Jackson Laboratory	N/A
Oligonucleotides		
sgDPP8: 5'-ATGATTTCATGTTTGTGAAG-3'	Okondo et al., 2017 ²⁰	N/A
sgDPP9: 5'-GGCCAACATCGAGACAGGCG-3'	Okondo et al., 2017 ²⁰	N/A
sgCARD8: 5'-TGACGATTGCGTTTGGTTCC-3'	Johnson et al., 2018 ²¹	N/A
sgNLRP1-hu: 5'-GGTGGTAGGAACGCCCCAC-3'	Ball et al., 2021 ²⁷	N/A

REAGENT or RESOURCE	SOURCE	IDENTIFIER
sgNLRP1-mu: 5'-GTGTAGGATGCCACAAATGA-3'	Chui et al., 2019 ⁸	N/A
sgCASP1-hu: 5'-CTAAACAGACAAGGTCCTGA-3'	Johnson et al., 2018 ²¹	N/A
sgCASP1-mu: 5'-TTAAACAGACAAGATCCTGA-3'	Okondo et al., 2017 ²⁰	N/A
qPCR-GAPDH-F: 5'-CAATGACCCCTTCATTGACC-3'	Common reagent	N/A
qPCR-GAPDH-R: 5'-GATCTCGCTCCTGGAAGATG-3'	Common reagent	N/A
Recombinant DNA		
pLEX_307	Gift from David Root	Addgene #41392
pInducer20 CARD8-HA PAM E274R	Sharif et al., 2021 ¹²	Addgene #169984
pInducer20 CARD8-HA PAM	Sharif et al., 2021 ¹²	Addgene # 169982
pLEX307_CARD8_FIIND_S297A_MYC	Sharif et al., 2021 ¹²	N/A
pLEX305-N-dTAG-CARD8-ZUC	Sharif et al., 2021 ¹²	Addgene #169990
pLEX_307 CASP1 Stop	Johnson et al., 2018 ²¹	N/A
pLEX_307 CARD8 FLAG	Johnson et al., 2018 ²¹	N/A
pLEX_307 mASC_hygro	This study	N/A
Software and algorithms		
GraphPad Prism Version 9	GraphPad Software	

Author Manuscript

Author Manuscript

Author Manuscript

Author Manuscript